1981

Energy Bands in Some Transition Metals.

Duane Giles Laurent
Louisiana State University and Agricultural & Mechanical College

LAURENT, DUANE GILES

ENERGY BANDS IN SOME TRANSITION METALS

The Louisiana State University and Agricultural and Mechanical Col. PH.D. 1981

PLEASE NOTE:

In all cases this material has been filmed in the best possible way from the available copy. Problems encountered with this document have been identified here with a check mark __✓__.

1. Glossy photographs or pages _____
2. Colored illustrations, paper or print _____
3. Photographs with dark background _____
4. Illustrations are poor copy _____
5. Pages with black marks, not original copy _____
6. Print shows through as there is text on both sides of page _____
7. Indistinct, broken or small print on several pages __✓__
8. Print exceeds margin requirements _____
9. Tightly bound copy with print lost in spine _____
10. Computer printout pages with indistinct print __✓__
11. Page(s) _____ lacking when material received, and not available from school or author.
12. Page(s) _____ seem to be missing in numbering only as text follows.
13. Two pages numbered _____. Text follows.
14. Curling and wrinkled pages _____
15. Other _____

ENERGY BANDS IN SOME TRANSITION METALS

A Dissertation

Submitted to the Graduate Faculty of the
Louisiana State University and
Agricultural and Mechanical College
in partial fulfillment of the
requirements for the degree of
Doctor of Philosophy

in

The Department of Physics and Astronomy

by
Duane G. Laurent
B.S., Southeastern Louisiana University, 1974
May 1981

To My Wife and Parents

ACKNOWLEDGEMENTS

The author is deeply indebted to Professor J. Callaway for his guidance and support during the course of this work. He also wishes to thank Dr. C. S. Wang without whom he would have surely perished amid the complexities of the band package. It is his pleasure to acknowledge Professor J. L. Fry for many stimulating discussions and for supplying the basic plotting software used in the Fermi surface investigations. In addition, he gratefully appreciates the good will supplied by the entire solid state group at LSU but particularly Professors S. P. Singhal, J. Kimball and A. K. Rajagopal and graduate students D. Bagayoko, A. Chatterjee and R. Ramana. The author also wishes to thank his parents, his wife Susan and his daughter Sarah. Without their love and support, this work would not have been possible.

Financial assistance for the publication of this dissertation was provided by the "Dr. Charles E. Coates Memorial Fund of the LSU Foundation donoted by George H. Coates." Research was supported in part by the National Science Foundation.

Lastly, the author acknowledges the System Network Computer Center (SNCC) staff at LSU for the computer facilities provided, Mrs. Martha Prather for typing this manuscript and Ms. Nancy Harris for graciously reinking and reprinting several plots specifically for this dissertation.

TABLE OF CONTENTS

	Page
ACKNOWLEDGEMENTS	ii
LIST OF TABLES	vi
LIST OF FIGURES	vii
ABSTRACT	ix
CHAPTER I. INTRODUCTION	1
CHAPTER II. THE SELF-CONSISTENT TIGHT-BINDING METHOD	7
A. The LCGO Method	7
B. Exchange-Correlation Potentials	11
C. Self-Consistency	14
CHAPTER III. THE ENERGY BANDS	20
A. Results and Comparisons	20
B. Density of States	27
C. Fermi Surface	31
CHAPTER IV. CALCULATED QUANTITIES	40
A. X-ray Form Factors	40
B. Compton Profiles	42
C. Optical Conductivity	45
CHAPTER V. CONCLUSIONS	54
REFERENCES	58
TABLES	64
FIGURES	83

Table of Contents (cont'd)

	Page
APPENDICES	108
A. Angle-Resolved Photoemission	108
B. Self-Energy Correction	113
VITA	117

LIST OF TABLES

Table		Page
I.	Absolute Energy Differences Between the KSG and VBH Exchange Potentials for Chromium	64
II.	Energy Differences for Selected States (Chromium)	65
III.	Energy Differences for Selected States (Vanadium)	66
IV.	Analysis of Kohn Anomalies of Chromium	67
V.	Chromium Fermi Surface Data	68
VI.	Vanadium Fermi Surface Data	69
VII.	X-Ray Form Factors of Chromium	70
VIII.	X-Ray Form Factors of Vanadium	71
IX.	Compton Profiles of Chromium	72
X.	Compton Profiles of Vanadium	73
XI.	Transition Thresholds of Vanadium	74
XII.	Optical Conductivity and Joint Density of States of Chromium	75
XIII.	Optical Conductivity and Joint Density of States of Vanadium	79

LIST OF FIGURES

Figure		Page
I.	Self-consistent Energy Bands of Chromium using the KSG Exchange Potential.....	86
II.	Self-consistent Energy Bands of Chromium using the VBH Exchange Potential.....	87
III.	Comparison of the VBH Energy Bands of Chromium with ARPE Data.....	88
IV.	Self-consistent Energy Bands of Vanadium using the KSG Exchange Potential.....	89
V.	Density of States of Chromium (KSG).....	90
VI.	Density of States of Chromium (VBH).....	91
VII.	Density of States of Vanadium (KSG).....	92
VIII.	Fermi Surface of Chromium (VBH)	
	A. Hole Surfaces Near H and N.....	93
	B. Electron "Jack".....	94
	C. Electron "Lenses".....	95
IX.	Fermi Surface Cross-Sections for Chromium (VBH)	
	A. (001) Plane.....	96
	B. (011) Plane.....	97
X.	Fermi Surface of Vanadium (KSG)	
	A. Hole Surface Surrounding Γ.....	98
	B. Jungle-Gym and Hole Surfaces Near N....	99
XI.	Fermi Surface (001) Cross-Section for Vanadium.....	100

List of Figures (cont'd)

Figure		Page
XII.	Spherically-Averaged Compton Profile of Chromium.....	101
XIII.	Anisotropy of the Compton Profile of Chromium.....	102
XIV.	Spherically-Averaged Compton Profile of Vanadium.....	103
XV.	Anisotropy of the Compton Profile of Vanadium.....	104
XVI.	Optical Conductivity of Chromium.....	105
XVII.	Optical Conductivity of Vanadium.....	106
XVIII.	Electron Energy-Loss Spectrum of Chromium.....	107

ABSTRACT

Self-consistent linear-combination-of-Gaussian-orbitals energy band calculations were performed for the two paramagnetic 3d transition metals, chromium and vanadium. The energy bands, densities of states and Fermi surfaces were obtained using the two most popular local-exchange-correlation potentials (Kohn-Sham-Gaspar and von Barth-Hedin) for chromium and the Kohn-Sham-Gaspar potential alone for vanadium. A comparison was made with the available experimental data. New interpretations for some of the neutron scattering data are made in the chromium case. Results are also presented for the Compton profiles and optical conductivities. These correlate well with the experiments if appropriate angular averages (for the Compton profile) and lifetime effects (for the optical conductivity) are included. The electron energy-loss spectrum, computed over the range 0-6.5 eV agreed well with experiment.

CHAPTER I

INTRODUCTION

In recent years, first-principles energy band calculations have been the subject of considerable interest in solid-state physics. Theoretical advances, particularly the techniques leading to self-consistency, have led to a better understanding of the electronic properties of transition metals, especially those properties derivable from bulk energy bands and wavefunctions. Simultaneously, developments in experimental techniques, such as angle-resolved photoemission, have allowed a more direct interaction between theory and experiment. Self-consistency has become very important since the d bands are sensitive to the asphericity caused by the crystal field.

This dissertation will report investigations of the energy bands and related properties of chromium and vanadium. These 3d transition metals form a very interesting pair. Both are paramagnetic (chromium at higher temperatures) having the body centered-cubic (B.C.C.) crystal structure and their lattice constants differ by only a few percent (5.4456 a.u. for chromium and 5.7448 a.u. for vanadium). Thus, the energy bands of chromium and vanadium are expected to be quite alike. However, as a first approximation, the presence of an additional electron in chromium shifts the Fermi energy

upward (the rigid-band model) which produces a very different Fermi surface topology than that found in vanadium. In addition to investigating these differences and those apearing in properties related to the energy bands, two of the popular local exchange potential models will be compared for chromium. These are the Kohn-Sham-Gaspar[1,2] (KSG) exchange potential and the von Barth-Hedin[3] (VBH) exchange-correlation potential.

Chromium is especially interesting because it exhibits antiferromagnetic behavior at low temperatures (below the Neél temperature of 312 °K). In addition, spin-density waves have been observed in this state. The situation is complicated by the fact that experiments have placed the wavelength of these waves at $(1-\delta)\ (2\pi/a)$ where δ varies with temperature from approximately 0.04 at room temperature to about 0.05 near 0 °K. Thus, the observed wavelength is incommensurate with the value expected for a perfect antiferromagnet $(2\pi/a)$. An exact calculation of such a system is extremely complex since the spin-density wave spectrum must be obtained from the maxima of the paramagnetic susceptibility function, $\chi(\vec{q})$. Computations of $\chi(\vec{q})$ have been limited by the rather severe approximations that are required.[4] However, Lomer[5] was able to explain the incommensurate behavior as a consequence of "nesting" in the paramagnetic Fermi surface. This nesting will be examined in some

detail along with the available neutron scattering data.

Both chromium and vanadium have been studied by a variety of experimental and theoretical techniques. The experiments include neutron scattering,[6-8] X-ray form factor determinations,[9-15] optical studies,[16-21] and Compton profiles.[22-26] There have also been magnetic susceptibility and magnetic field experiments[27-30] on antiferromagnetic chromium. Even the effects of alloying have been investigated.[31,17] Recent advances in the interpretation of angle-resolved photoemission (ARPE) data[32] have allowed experimental verification (at least to a limited degree) of the actual energy bands in the bulk.

Among the methods of band structure calculations that have been used to investigate chromium and vanadium are the tight-binding (LCAO and LCGO) method,[33] the Augmented Plane Wave (APW) scheme,[34,35,4] the KKR (Green's function) approach,[36,37] the Orthogonalized Plane Wave (OPW) method[38] and the Linear Muffin-Tin Orbitals (LMTO) method.[39] Two groups[36,39] have reported results for the (commensurate) antiferromagnetic phase of chromium. The first method used to investigate energy bands was the plane wave expansion. However, a very large number of plane waves were needed to represent the core states. The OPW method averted this problem by using tightly-bound functions for the core in

conjunction with plane waves that were made orthogonal to the core for the valence states. In their usual forms, the APW, KKR and LMTO methods all employ the "muffin-tin" approximation in which the crystal potential is assumed to be spherically symmetric inside spheres centered on each atomic site and takes on a constant value outside of these spheres. In the KKR method, the wavefunctions are expanded in terms of spherical waves (products of spherical harmonics and radial wave functions). Then the Schrodinger equation is transformed into a homogeneous integral equation. Finally, with the application of a variational procedure, the dispersion relation is obtained as the solution of a secular equation. The APW approach also involves an expansion of the wavefunction in spherical waves, but only on the interior of the spheres. In the region between the spheres, a plane wave expansion is used instead. Then, the expansion coefficients are varied such that the logarithmic derivatives of the wavefunction are continuous across the sphere boundary. In the LMTO scheme, an expansion similar to the KKR method is used with the exception that muffin-tin (MT) orbitals (linear combinations of spherical waves and their first derivatives) are used in the interior of the atomic spheres rather than spherical waves and solutions to the Laplace equation instead of plane waves in the region between the spheres.

This method combines some of the best features of the APW and KKR methods but still suffers because of the muffin-tin approximation used in generating the potentials.

This dissertation is organized as follows: In Chapter II, we outline the self-consistent linear combination of Gaussian orbitals (LCGO) method. Section A examines the approximations and modifications made to the basic tight-binding method. The various local exchange-correlation potential models are discussed in Section B. The importance of self-consistency to current band structure calculations as well as its application in the tight-binding method appear in Section C.

Chapter III examines the energy bands of chromium and vanadium in great detail. In Section A, the energy bands are compared to other calculations and, for chromium, to recent angle-resolved photoemission data. The densities of states discussed in Section B were computed using the linear analytic tetrahedron method. The Fermi surfaces are compared with experiment in Section C. The amount of Fermi surface that "nested" was found to be large in chromium and small in vanadium. The available neutron scattering data for chromium is interpreted in terms of extremal orbits and "nesting" of the various portions of the Fermi surface.

The various properties derivable from the bulk energy bands are discussed in Chapter IV. The charge distributions

as measured by the X-ray form factors are compared in Section A to other calculations and to the various experiments. The electron momentum distributions are examined via the Compton scattering profiles in Section B. The frequency-dependent interband optical conductivities, presented in Section C, required the inclusion of phenomonological relaxation times to provide better agreement with experiment. Since the electron energy-loss spectrum is simply related to the optical conductivity, it too has been computed and compared to experiment.

The general conclusions are stated in Chapter V. Appendix A discusses the theory behind angle-resolved photoemission and the method used to interpret the energy-distribution curves to obtain a picture of the actual bulk energy bands. Appendix B contains information about the electron self-energy correction for excited states.

CHAPTER II

THE SELF-CONSISTENT TIGHT-BINDING METHOD

This chapter consists of three sections. In Section A, the LCGO method is discussed along with the choice of basis set and the construction of the one-electron potentials. Section B contains a discussion of the local exchange potentials used in this work and self-consistency will be outlined in Section C.

A. The LCGO Method

The basic tight-binding method seeks the solution to the problem of an electron in a solid by attempting to solve the single-particle wave equation

$$(-\nabla^2 + V(\vec{r}))\psi_n(\vec{k},\vec{r}) = E_n(\vec{k})\psi_n(\vec{k},\vec{r}) \qquad (1)$$

The band index, n, implicitly contains the spin direction if a ferromagnetic calculation is desired and $V(\vec{r})$ contains the Coulomb potential as well as a (spin-dependent) exchange-correlation term

$$V(\vec{r}) = -2Z \sum_{\mu} |\vec{r}-\vec{R}_{\mu}|^{-1} + 2\int \frac{\rho(\vec{r}')}{|\vec{r}-\vec{r}'|}\, d\vec{r}' + V_x(\vec{r})$$

Here Z is the atomic number of the nucleus, $\rho(\vec{r})$ is the electronic charge density and $\vec{R}_{\mu}$ is the position vector

of the μ^{th} atomic site. The units used throughout this work are tyical of those found in band structure calculations ($\hbar$=c=1, e^2=2, m=½). Because the non-local nature of exchange and correlation poses an enormous problem to band structure calculations, various local models have been proposed. These will be discussed in detail in the following section.

The wave equation (1) is solved by expanding the exact wavefunction $\psi_n(\vec{k},\vec{r})$ in terms of a suitable basis set. The functions in the basis set must satisfy Bloch's theorem

$$\phi_i(\vec{k},\vec{r}+\vec{R}_\mu) = \phi_i(\vec{k},\vec{r})$$

and can therefore be written as

$$\phi_i(\vec{k},\vec{r}) = 1/\sqrt{N} \sum_\mu e^{i\vec{k}\cdot\vec{R}_\mu} u_i(\vec{r}-\vec{R}_\mu) \qquad (2)$$

where the localized functions, $u_i(\vec{r})$ are assumed to be normalized but not necessarily orthogonal. In the tight-binding method as originally formulated by Bloch,[40] these localized functions were chosen to be atomic orbitals, hence the name linear-combination-of-atomic-orbitals (LCAO) which has become synonomous with this method. However, the presence of three-center integrals due to the multi-center potential terms proved to be a major

disadvantage. Lafon and Lin[41] replaced the potential terms with a Fourier series over reciprocal lattice vectors

$$V(\vec{r}) = \sum_{\vec{K}} V(\vec{K})\ e^{i\vec{K}\cdot\vec{r}}$$

which reduced the problem to two-center terms only. If the localized functions are then chosen to be Gaussian, the integrals required for the Hamiltonian and overlap matrix elements can be expressed analytically. While this procedure does require a larger basis set than the atomic-orbitals expansion, the analytic evaluation of the integrals drastically reduces the amount of computation required. The localized functions have the form

$$u_i(\vec{r}) = R_{n\ell}(r)K_{\ell m}(\theta,\phi)$$

where $K_{\ell m}(\theta,\phi)$ is a Kubic harmonic and

$$R_{n\ell}(r) = (2(2\alpha_{n\ell})^{\ell+\frac{1}{2}}/\Gamma(\ell+1/2))^{\frac{1}{2}}\ r^{\ell-1}\ e^{-\alpha_{n\ell}r^2}$$

is a radial wavefunction. The basis set used in this work consists of thirteen s-type, ten p-type, five d-type and one f-type function, forming Hamiltonian and overlap matrices which are of order 75.

Once the basis set has been chosen, we perform the expansion

$$\psi_n(\vec{k},\vec{r}) = \sum_j C_{jn}(\vec{k})\,\phi_j(\vec{k},\vec{r})$$

and then substitute this expression into equation (1). The resulting matrix equation

$$\sum_m (H_{nm}(\vec{k}) - E_n(\vec{k})\ S_{nm}(\vec{k}))C_{nm}(\vec{k}) = 0 \qquad (3)$$

can then be solved by standard techniques for the energies $E_n(\vec{k})$ and the expansion coefficients $C_{nm}(\vec{k})$. In equation (3), we have used the definitions

$$H_{ij}(\vec{k}) = \langle\phi_i(\vec{k},\vec{r})\,|\hat{H}|\,\phi_j(\vec{k},\vec{r})\rangle$$

$$S_{ij}(\vec{k}) = \langle\phi_i(\vec{k},\vec{r})\,|\,\phi_j(\vec{k},\vec{r})\rangle$$

where $\hat{H}$ is the Hamiltonian operator. The use of Gaussian functions and Fourier expansions of the potential terms in this way allows us to write all required integrals as a linear combination of integrals of a simple cosine function

$$\langle u_i(\vec{r}-\vec{A})|\cos\,\vec{K}\cdot\vec{r}\,|u_j(\vec{r})\rangle$$

following the procedures of Chaney and Dorman.[42] The resulting expression, involving binomial expansions in Hermite polynomials, is very complex and is reported in Wang and Callaway.[43]

B. Exchange-Correlation Potentials

As stated in the previous section, a local potential that includes exchange and preferably some correlation is very desirable. The first such model to be proposed was due to Slater[44] and consisted of the very simple relation.

$$V_x(\vec{r}) = -6(3\rho(\vec{r})/(8\pi))^{**}(1/3) \qquad (4)$$

This ptoential was later examined by Kohn and Sham[1] and by Gaspar[2] who concluded that, under their assumptions, the exchange potential has the form

$$V_x(\vec{r}) = -4(3\rho(\vec{r})/(8\pi))^{**}(1/3) \qquad (5)$$

which is exactly 2/3 of the value obtained by Slater. Both of the above results were obtained for a system consisting of a free-electron gas with a uniform neutralizing distribution of positive charge. Some effort to unify these viewpoints produced what is now called the Xα potential

$$V_{x\alpha}(\vec{r}) = -6\alpha(3\rho(\vec{r})/(8\pi))^{**}(1/3) \qquad (6)$$

in which α can take on a value between 2/3 and 1 and in some calculations is even regarded as a variational

parameter. The corresponding problem of the local exchange potential for an electron in a real solid has not been solved and hence no "correct" value of α exists. However, many investigations have implied that a value near 2/3 produces satisfactory results in a self-consistent calculation while a value near 1 is appropriate when self-consistency is not desired. The ferromagnetic analog of the $X\alpha$ potential

$$V_{X\alpha,\sigma}(\vec{r}) = -6\alpha(3\rho_\sigma(\vec{r})/(4\pi))^{**}(1/3)$$

was obtained by Rajagopal and Callaway[45] and has been used with much success in recent studies of iron[46] and nickel.[47]

In the past few years, several newer potentials have emerged which attempt to deal with correlation in more detail. The most popular is the model proposed by von Barth and Hedin[3] and Hedin and Lundquist.[48] This potential can be written in the form

$$V_{Xc,\sigma}(\vec{r}) = -6(A(\rho)\rho_\sigma^{1/3}(\vec{r}) + B(\rho)) \qquad (7)$$

where A and B are explicit functionals of the total charge density $\rho(\vec{r})$. Prescriptions for A and B may be obtained from the above references and in the paramagnetic limit, equation (7) reduces to

$$V_{Xc}^{p}(\vec{r}) = -\frac{2}{\pi}\left(\frac{9\pi}{4}\right)^{1/3}\frac{1}{r_s} - .0504\ \ell n(1 + 30/r_s)$$

where

$$r_s = (3/4\pi\ \rho(\vec{r}))^{1/3}\ .$$

However, there were several points in the derivation of this potential which did not have the most solid theoretical basis. The results were subsequently re-examined by Rajagopal, Singhal and Kimball[49] who obtained a potential with the same functional form as equation (7) but with slightly different constants in the prescriptions for A and B. Although this potential (RSK) is on more solid ground than that of von Barth and Hedin (VBH), recent comparative tests involving self-consistent calculations for both nickel[50] and copper[51] have detected no difference between the two in terms of energy differences or Fermi surfaces.

In the work presented in this dissertation, the Xα potential with $\alpha = 2/3$ (KSG potential) was initially used for both chromium and vanadium since it has been in use for a number of years and has proven to give very reliable and consistent results. In addition, it was desirable to have a side-by-side comparison between the various forms of local-exchange-correlation potentials and so the complete calculation of the energy bands was redone for chromium using the VBH exchange potential.

Janak, et al.[52] reported one such comparison performed on copper using several different values of α in the Xα formalism, the Chodorow[53] potential and the VBH potential. As expected, their results showed little difference between the ab initio potentials. However, copper is a rather simple metal and a more complex material might show more significant effects. In any case, at metallic densities, corelation effects are expected to be much smaller (typically a factor of 5) than exchange effects.[92]

C. Self-Consistency

Band structure calculations must use a realistic potential in order to obtain realistic results. The usual procedure is to begin with a superposition of atomic charge densities and then to use Poisson's equation

$$\nabla^2 V(\vec{r}) = 8\pi\rho(\vec{r}) \qquad (8)$$

to generate the needed crystal potential. Examination of the Fermi surface obtained from an $\alpha = 2/3$ non-self-consistent energy band calculation for chromium reported by Fry, et al.[54] shows that the results are totally non-physical. This same behavior can also be expected for any other quantities calculated from such energy bands. Thus self-consistency, the process by which the charge is redistributed in response to exchange and correlation

in the solid, is indispensable if the band structure is to be at all realistic.

Self-consistency is best achieved by an iterative process. The procedure used in the tight-binding method was first introduced by Callaway and Fry.[55] Initially the crystal potential is generated using a superposition of charge densities obtained from a free-atom calculation. Wachters[56] has calculated the wavefunctions for many free atoms using a basis of Gaussian orbitals. However, since population analysis of the transition metals indicates a shift in population from the 4s level to the 3d level in the solid, a $3d^n\ 4s^1$ configuration is used (n = 5 for chromium, n = 4 for vanadium) rather than the neutral-atom population $3d^{n'}\ 4s^2$ (n' = 4 for chromium, n' = 3 for vanadium). The resulting charge distributions determine the potentials and then the Fourier coefficients of those potentials are obtained. These Fourier coefficients are used to generate a set of integrals of the Coulomb and exchange potentials, the kinetic energy and the overlap between the functions in the Gaussian basis set. These integrals are then combined to form the corresponding matrix elements according to the rule

$$O_{ij}(\vec{k}) = \sum_{\mu} e^{-i\vec{k}\cdot\vec{R}_{\mu}} \int u_i^*(\vec{r}-\vec{R}_{\mu})\ \hat{O}\ u_j(\vec{r})\,d\vec{r}$$

where $\hat{O}$ is an operator belonging to the above set.

At this point, the iterations begin, each consisting of the following steps. First, the energies and wavefunctions are generated at each $\vec{k}$-point in a mesh defined in the irreducible wedge (1/48 of the first Brillouin zone) using the potentials from the last iteration (if any). From this band structure, a Fermi energy is determined. Then, corrections to the leading Fourier coefficients of the charge density are generated in the following manner. The charge density resulting from the wavefunctions obtained in the i^{th} iteration is

$$\rho^{(i)}(\vec{r}) = \sum_{n\vec{k}} |\psi_n(\vec{k},\vec{r})|^2$$

where the sum is carried out over all occupied states. After expanding the wavefunctions in terms of the individual Gaussians, the Fourier coefficients of the charge density become

$$\rho^{(i)}(\vec{K}_s) = \frac{1}{N\Omega} \sum_{nij} \int d\vec{k}\; C^*_{ni}(\vec{k})\; S_{ij}(\vec{k},\vec{K}_s)\; C_{jn}(\vec{k})$$

The <u>generalized overlap integrals</u> used in this result

$$S_{ij}(\vec{k},\vec{K}_s) = \Sigma\; e^{-i\vec{k}\cdot\vec{R}_\mu} \int u_i^*(\vec{r}-\vec{R}_\mu)\; e^{i\vec{K}_s\cdot\vec{r}}\; u_j(\vec{r})\,d\vec{r}$$

are related to the usual overlap integrals by

$$S_{ij}(\vec{k}) = S_{ij}(\vec{k},\vec{K}_s = 0)$$

Then, the change in the charge density is

$$\Delta\rho^{(i)}(\vec{K}_s) = \rho^{(i)}(\vec{K}_s) - \rho_o(\vec{K}_s)$$

where $\rho_o(\vec{K}_s)$ is the result of the superposition of atomic charge densities (i.e., the zeroth iteration).

Once the correction to the charge density has been found, the potentials must be altered to compensate for the charge redistribution. The Fourier transform of the Coulomb potential (equation (8)) is

$$V_c(\vec{K}_s) = -8\pi\ \rho(\vec{K}_s)/K_s^2$$

so that the change in $V_c(\vec{K}_s)$ is <u>linear</u> in $\Delta\rho(\vec{K}_s)$. For the exchange potential(s), however, the situation is much more complex. The result can be written as

$$\Delta V_{x,\sigma}(\vec{K}_s) = \sum_t DV_{x,\sigma}(\vec{K}_s-\vec{K}_t)\,\Delta\rho_\sigma(\vec{K}_t)$$

where $DV_{x,\sigma}(\vec{K}_s)$ is the Fourier component of the <u>derivative</u> of the exchange potential being used with respect to $\rho_\sigma(\vec{K}_s)$. This expression is independent of the <u>form</u> of the exchange potential used in the calculation.

The Fourier coefficients of the charge density for large-magnitude reciprocal lattice vectors describe the charge density deep in the core and have been observed not to change during the self-consistent cycle. In fact, only the first 10-15 coefficients change appreciably. However, to be sure that we have included a sufficient number, we compute and save the changes for the first 40 reciprocal lattice vectors.

Early self-consistent calculations often reported that the iterations diverged. This seems to be an artifact of the first-order scheme used to correct the charge density since convergence is achieved if the initial and final chage distributions are sufficiently close together (about one percent). Convergence can be assured by averaging the correction terms from the current and previous iterations according to the rule

$$\Delta\rho^{(i)} \leftarrow (1-\beta)\Delta\rho^{(i-1)} + \beta\Delta\rho^{(i)}$$

If β is too large, convergence will not result while if it is too small, the rate of convergence will be slowed. A choice of 0.3 provided a satisfactory rate in this work. Then, after the results have stabilized to about 0.01 percent, the value of β is increased to 1 over several iterations to insure that the results have indeed converged.

In order to use the available computer time most efficiently, the first 16 iterations were performed using a rather coarse mesh (30 points in the irreducible wedge). This produced correction terms that had stabilized to about 0.001 Rydberg. Then the number of points was increased to 140 and seven additional iterations were carried out. This procedure enabled us to obtain correction terms converged to better than 0.0001 Rydberg for both chromium and vanadium.

CHAPTER III

THE ENERGY BANDS

This chapter also contains three sections. The first, Section A, compares the energy bands obtained with the KSG potential with those obtained with the VBH potential for chromium. Then the calculated band structures of both chromium and vanadium are compared with other calculations. In addition, the chromium VBH results are comapred to recent ARPE experiments. The densities of states, discussed in Section B, were obtained using the Gilat-Raubenheimer[57] method with a linear interpolation scheme (the linear analytic tetrahedron method). The electronic specific heats are also examined. Section C presents the Fermi surfaces and discusses "nesting" and the spin-density wave interpretation.

A. Results and Comparisons

Once the self-consistent corrections have been obtained, they are used to regenerate the integrals so that they too reflect the charge redistribution. Then the final (self-consistent) band structure is calculated at a large number of points (506 for both chromium and vanadium) in the irreducible wedge.

Chromium

The self-consistent energy bands of chromium obtained using the KSG potential are displayed along the axes of high symmetry in Figure I. The corresponding results with the VBH exchange-correlation potential are shown in Figure II. A comparison of the shifts of selected states at points of high symmetry is shown in Table I. The results are quite similar with the VBH bands lying lower than their KSG counterparts by an almost constant 0.15 Rydberg. Closer examination reveals that the s- and p-like states are about 0.145 Rydberg lower while the d-like states are nearly 0.154 Rydberg lower. The result is an overall compression of the bands by about 8 milliRydberg which may be attributed to correlation effects. Figures I and II resemble the earlier results for paramagnetic chromium,[4,33,36-40,54,58,59] except for the levels near the Fermi energy at the N point. The calculations using methods that can be most closely compared to this work[4,33,36-38,54] are shown in Table II. The augmented plane wave (APW) band structure reported by Gupta and Sinha[4] used the Xα exchange potential with $\alpha = 1$ and was not self-consistent. Thus agreement with their work is not expected. Asano and Yamashita[36] examined both the para- and antiferromagnetic phases of chromium using the self-consistent Green's function (KKR) method. Their calculation included exchange in the same

manner as Gupta and Sinha but they added an additional correlation term. A hybridized tight-binding and orthogonal plane wave (OPW) technique was used by Yasui, et al.[38] and was iterated to self-consistency using two different values of α (1.0 and 0.725) in the Xα exchange potential. They found that α = 0.725 gave a more realistic Fermi surface and spin density wave parameters than α = 1.0 in agreement with our prior statements. A recent calculation for the commensurate antiferromagnetic phase has been reported by Skriver[39] who employed the same VBH exchange-correlation potential used in this work.

An earlier calculation by Rath and Callaway[33] using the same basic method as this work is included for the sake of comparison. One of the principal reasons for this calculation was to try to resolve the question about the relative positions of the states N_1, N_1' and N_4. Since the Rath and Callaway results were published, the computer programs in use at LSU have been significantly improved to the extent that they too have been published.[43] The new calculations have larger s- and p-type basis sets and also include an f-type function. In addition, the treatment of the exchange potential in the interstitial region has been improved so that the Fourier coefficients of that potential should be more realistic. It is thought that the increased variational freedom in this study

accounts for most of the differences since the position of the state N_1' (primarily p-like) was affected the most. However, note in Table II that the position of this state appears to be highly dependent upon the form of the exchange potential. Thus, this work failed to resolve the controversy concerning the states at the N point.

The occupied d bandwidth, measured by $(E_f - H_{12})$, is 4.25 eV for the KSG bands and 4.20 eV for the VBH results. Johansson, et al.[60] obtained a total occupied band width $(E_f - \Gamma_1)$ of nearly 7.0 eV using angle-resolved photoemission which is slightly smaller than our values 7.72 eV (7.62 eV). The total d bandwidth $(H_{25}' - H_{12})$ was estimated to be 6.2 eV by McAllister, et al.[61] on the basis of X-ray emission and measurements of the appearance potential while we obtain 6.63 eV (6.53 eV).

A new interpretation has recently been given to the electron energy-distribution curves obtained in angle-resolved photoemission experiments (see Appendix A). If a free-electron final state is assumed, the curves may be used to generate an actual picture of some of the bulk energy bands. Only those bands allowed by symmetry to serve as an initial state for a free-electron final state can be observed. This is not a serious problem since many energy bands will usually satisfy that criterion and this technique is such a tremendous advance that this problem can be overlooked. However,

we do need to know something about the wavefunctions of the electrons being ejected from the sample in the ARPE experiment. The usual procedure is to use a free-electron-like (s-like) state from a band structure calculation. Such an interpretation was carried out by Johansson, et al. for antiferromagnetic chromium and the results agreed reasonably well with the bands of Asano and Yamashita. However, the final-state energies used in that interpretation were obtained from the Hartree calculation of Fry, et al.[54] which gave bands that were unreasonably wide (9.0 eV for the d bandwidth and 9.7 eV for the total occupied bandwidth). Thus, the curves of Ref. 60 were reinterpreted using the Σ_1 band (s-like) from our VBH band structure which lies in correct range of photon energies (15-25 eV). The results are shown in Figure III and are in reasonable agreement with our bands. The interesting point is that these results are not very different from those using the Hartree final state. In Figure III, the bands along the G axis ($\overline{NH}$) were folded over those along the Σ axis ($\overline{\Gamma N}$) to approximate a (commensurate) antiferromagnetic band structure since the ARPE data was obtained for a sample in that state.

Vanadium

The self-consistent energy bands for vanadium using the KSG exchange potential are shown along high symmetry axes in Figure IV. As expected, the results are very similar to the chromium bands previously discussed. In fact, if one were to simply shift the Fermi energy to a position just below the Γ'_{25} energy (in effect, removing one electron) in the chromium bands, the results would be almost indistinguishable from Figure IV. There are differences, of course, such as the states N_1 and N'_1 which are farther apart (0.063 Rydberg) that they are in chromium (0.0004 Rydberg). Table III compares our results with the calculations reported in the literature.[34,35,37,38,62-64] However, there is much less data published about vanadium than about chromium. The APW results of Papaconstantopoulos, et al.[34] were self-consistent and used both the Slater ($\alpha = 1$) and the KSG exchange potentials. They also used the Slater in a non-self-consistent band structure which agreed reasonably well with the self-consistent KSG bands although the details are not identical. This is consistent with our previous statements about the desired value of α. Their self-consistent Slater exchange calculation produced a band structure that was too narrow when compared to other calculations and to experimental results. In the later results of Boyer, et al.,[35] the value of α

suggested by Schwarz[65] (.71556) was used. The agreement they obtained with experiment was not as good as their KSG bands. Yasui, et al.[38] carried out a self-consistent calculation using a modified tight-binding and orthogonalized plane wave method, also examining both the full Slater and the Xα (with $\alpha = .725$) exchange potentials. They also found that the $\alpha = .725$ results were better (in terms of agreement with experiment) than the Slater exchange bands. A KKR calculation by Wakoh and Yamashita[37] examined vanadium as well as chromium using so-called "state-dependent" potentials. In this scheme, the potential is different for the different symmetries of d states. However, this is not an ab initio procedure as it contains some parameters which are determined from the experimental Fermi surface.

Overall, the bandwidths are about 10 percent smaller than they were for chromium. The occupied d band width, now given by $E_f - N_1$, is 3.1 eV (as compared to 3.0 eV, obtained from the photoemission measurement of Eastman[66]). The total occupied bandwidth ($E_f - \Gamma_1$) is 6.4 eV which may be compared to the value 6.3 eV measured by Fischer[67] and Hague and Bonnelle.[68] The total d band width, including unoccupied states, is 7.0 eV ($N_3 - N_1$).

B. Density of States

The density of states, given by

$$N(E) = \frac{\Omega}{(2\pi)^3} \sum_n \int_{BZ} \delta(E - E_n(\vec{k}))\, d\vec{k}$$

measures the number of states per unit energy. Here Ω is the unit-cell volume and the integral is to be carried out over the Brillouin zone. In the scheme of Gilat and Raubenheimer,[57] this integral is changed into a surface integral over the Fermi surface

$$N(E) = \frac{\Omega}{(2\pi)^3} \sum_n \int_{FS} dS_{\hat{k}} / |\vec{\nabla}_{\vec{k}} E_n(\vec{k})|$$

Then $\vec{k}$-space is filled with non-overlapping tetrahedra which are identical except for orientation in space. If the integrand is then assumed to be linear within each tetrahedron, the integral can be expressed analytically (linear analytic tetrahedron method). Of course, this technique works only if the number of tetrahedra used allows the above assumption to be approximately valid. This lower limit seems to be about 50-75 points so that our final bands do indeed satisfy that criterion.

Chromium

The density of states for the KSG potential shown in Figure V and that for the VBH potential in Figure VI are very similar to those obtained in Ref. 38 and Ref. 54 and virtually identical to that of Rath and Callaway.[33] Note that the Fermi energy lies near the bottom of the minimum in the d-band complex. This is one of the characteristics of a material that is expected to exhibit antiferromagnetic behavior. Figure VI also shows the integrated density of states which counts the number of electrons. The density of states at the Fermi energy for the KSG potential is 9.14 states/atom-Rydberg while it is 9.41 states/atom-Rydberg for the VBH potential. The electronic specific heat is related to the density of states at the Fermi energy by

$$\gamma_e = \frac{1}{3} \pi^2 k^2 N(E_f)$$

Thus, the values we obtain for the specific heat are 1.58 (1.62) mJ/mole $°K^2$ for the KSG (VBH) exchange potential. The experimental result,[69] 1.5 mJ/mole $°K^2$, is deceptively close to the above values. Unfortunately, this experiment was performed on a sample in the <u>antiferromagnetic</u> state. Therefore, the above values should not be compared directly. While it is not possible to

have paramagnetic chromium at temperatures below the Neél temperature (312 °K), alloys of chromium and vanadium are paramagnetic. Since chromium and vanadium are so closely related, we should be able to extrapolate the results from measurements of dilute alloys. The result[69] of such an extrapolation is 2.9 mJ/mole $°K^2$. While this value seems to be much too large, it must be remembered that the experiments include the contributions to the specific heat from the electron-phonon interaction. When this interaction is treated in second-order perturbation theory, the density of states at the Fermi energy and hence the specific heat is modified by a factor $(1 + \lambda)$,[70] called the phonon renormalization factor. The factor thus obtained is $(1 + \lambda) = 1.83$. This is consistent with values reported for iron[46] and nickel.[47]

An alternate procedure is to examine the antiferromagnetic density of states. The gaps that appear relative to the paramagnetic energy bands destroy large sections of the Fermi surface which decreases $N(E_f)$ by a corresponding amount. Fry, et al.[71] estimate a 30 percent reduction in $N(E_f)$ on the basis of a perturbation calculation assuming an incommensurate spin density wave while Skriver[39] and Asano and Yamashita[36] agree on a value of 29 percent for the commensurate phase. Therefore, a 29 percent reduction in our (paramagnetic)

density of states at the Fermi energy should be a reasonable approximation to the antiferromagnetic value. Application of this reduction to our calculated specific heats produces values of 1.12 and 1.15 mJ/mole $°K^2$. When these are compared to the (antiferromagnetic) experimental result,[69] (1.5 mJ/mole $°K^2$), the phonon enhancement factor becomes 1.32, in reasonably good agreement with the value 1.49 obtained from the calculation of Skriver. Thus, the electron-phonon interaction appears to be significantly weakened by the spin-density waves present in the antiferromagnetic state.

Vanadium

The density of states presented in Figure VII was computed using the KSG exchange potential. Note that it is virtually indistinguishable from the corresponding curve for chromium except for the position of the Fermi energy. Instead of lying in a minimum, the Fermi energy lies near a maximum in the d-band complex. This gives a value of 25.03 states/atom-Rydberg for the density of states at the Fermi energy and consequently $\gamma_e = 4.34$ mJ/mole $°K^2$. In this case, the experimental value[69] ($\gamma_e = 9.92$ mJ/mole $°K^2$) should be directly compared to the value obtained above since vanadium is not antiferromagnetic. Thus, the phonon renormalization factor is found to be $(1 + \lambda) = 2.29$. Unlike chromium, this

is much larger than the value (1.6) which is conventionally attributed to phonon effects. The discrepancy is not restricted to our results, however, as Boyer et. al.[35] found factors of 2.84 for the KSG potential and 2.22 for an Xα calculation with $\alpha = 0.71556$.

C. Fermi Surface

The Fermi surface is the constant-energy surface whose energy value is the Fermi energy. The topology of the Fermi surface may be best understood by examining projective plots of the three-dimensional Fermi surface. When measuring the nesting parameters and cross-section areas, contour plots in planes cut through $\vec{k}$-space in various orientations and positions are most useful.

A few words about the scheme used to number the energy bands is in order. First note that we are concerned with only 6 bands. At the Γ point, these are the five d-like states and the single s-like state which are numbered from 1 to 6 in order of increasing energy. Thus, band 1 corresponds to Γ_1, bands 2, 3 and 4 to Γ'_{25} and bands 5 and 6 to Γ_{12}. The only objection to this scheme is that symmetry is not conserved during band crossings. For example, along the G axis near H, band 2 is of G_4 symmetry while band 3 is of G_3. However, near N, band 2 is the G_3 state while band 3 is the G_4 state. While this objection is serious, this scheme

appears to be the only unique one. When examining all Fermi surface dimensions, the point at which the band crosses the Fermi energy was determined with a four-point Aitken's interpolation scheme.

"Nesting" occurs when portions of the Fermi surface are parallel to one another. In this work, we will refer to the nesting as either "strong" (having a large joint density of states) or "weak" (having a small joint density of states). Following the treatment of Lomer,[5] we note that the main effect of a small-magnitude periodic perturbation (such as a spin-density wave in an antiferromagnetic system) is to mix wavefunctions whose $\vec{k}$-vectors differ by the vector ($\vec{Q}$) of the perturbation. This can be observed by noting that, from perturbation theory, the change in the energy is of second order in the perturbation while the change in the wavefunction is of <u>first</u> order. Thus, the greatest effect will be seen when there are a large number of available states whose $\vec{k}$-vectors differ by $\vec{Q}$. Therefore, we should look for large portions of the Fermi surface that "nest" together (i.e., strong nesting). Of course, this may not predict the observed value of $\vec{Q}$, since the allowed $\vec{Q}$ values in the spin-density wave spectrum are the zeroes of the inverse of the susceptibility function $\chi(\vec{q})$. In such a calculation, matrix element effects might substantially modify the position of these zeroes. However,

the "nesting" approach does seem to give reasonable agreement with experiment and it is quite simple to apply since it does not involve intricate calculations.

In order to determine the area of the features at N and X, the coordinates of points on the Fermi surface were determined by interpolation. Then these points were fit to ellipses aligned along the symmetry axes. The semi-major axes, extracted from the least-squares fitting parameters, determine the area. In all cases, the uncertainties in this least-squares procedure was less than 2 percent. The areas for energies Ef+ε and Ef-ε were also determined using ε = 0.001 Rydberg. Then, the derivative of the area with respect to energy, needed for the effective mass calculation, was approximated by

$$(dA/dE)_{E_F} \approx (A(Ef+\varepsilon) - A(Ef-\varepsilon))/2\varepsilon$$

Chromium

The projective plots of the Fermi surface of chromium are displayed in Figure VIII. The first two bands are completely filled while band 6 is unoccupied. Band 3 forms a set of (closed) hole pockets at H and at N as shown in Figure VIII(a). The next higher-energy band (4) is a curious object known as the electron "jack" (Fig. VIII(b)) from its resemblance to the

child's toy. Finally, band 5 generates a set of electron surfaces having the shape of "lenses" or "caps". It is interesting to note that in some calculations (Ref. 54 for example) these lenses are absent. Presumably, this is due to the exchange potential used there. The resemblance of these figures to the sketches of Mattheis and to Lomer's model is apparent.

The phonon dispersion relations can be conveniently examined by measuring the inelastic scattering of neutrons. Kohn[72] first postulated that the interaction between lattice vibrations and the conduction electrons might give rise to anomalies in the phonon spectrum. These Kohn anomalies occur at phonon wave vectors equal to the extremal dimensions of portions of the Fermi surface. Roth, et al.[73] subsequently showed that "nesting" of Fermi surface features can also lead to these anomalies.

A comparison of our results with the experimental neutron scattering data[7,8] is summarized in Table IV. The "nesting" was quite strong, indicating the existence of large Kohn anomalies. Muhlstein interpreted the anomalies in this data in terms of both extremal dimensions of a feature of the Fermi surface (the first two entries in Table IV) and of "nesting" of these rather large portions of the Fermi surface. However, he interpreted the Kohn anomaly along $\overline{\Gamma H}$ (near H) as the

result of nesting of the body of the electron jack with the holes at H along the (001) axis. We feel that the data is better explained if that anomaly is associated with the extremal dimension of the electron jack, leaving the nesting to account for the wave vector of the spin density wave. The strength of the nesting that occurs for chromium can be observed in Figure IX which contains cross-section (contour) plots of the complete Fermi surface (all three bands). Figure IX(a) is a (001) plane cut through the origin and the corresponding (011) plane is shown as Figure IX(b).

The de Haas-van Alphen effect can also provide information about the size (and shape to a limited extent) of the Fermi surface features. The cross section area (A) of a feature (in a plane perpendicular to the applied magnetic field) is related to the observed dHvA frequency by the formula

$$f = (\hbar c/2\pi e)\, A$$

Graebner and Marcus[30] chose the dimensions of ellipsoids centered at N and at X (the midpoint of the Δ axis in the paramagnetic Brillouin zone) which best reproduce the observed dHvA frequencies. The resulting semi-axes, shown in Table V, provide a ± 10 percent fit for the holes at N and ± 20 percent fit for the electron balls

at X (the ball dimensions had to be deduced from the data given in Reference 30 as they are not explicitly given there). The lack of good agreement may be attributed in part to the different effective areas of the closed orbits in the paramagnetic system as compared to the open orbits measured in the (antiferromagnetic) crystal.

The cyclotron effective mass ratio (the effective mass divided by the free-electron mass) can be obtained during de Haas-van Alphen measurements. This ratio is related to the energy derivative of the cross-section area of a Fermi surface feature by the formula[34]

$$(m^*/m) = (\hbar^2/2\pi m)\ (dA/dE)_{E_F}$$

The derivative is estimated as described above. The results (in Table V) show that the VBH potential gives slightly better results than the KSG potential when compared to the work of Graebner and Marcus.

Vanadium

The Fermi surface of vanadium is depicted in the projective plots of Figure X. Like chromium, band 1 is completely full while the top three bands are empty. The second band is occupied everywhere except near the center of the zone, forming a closed (hole) octahedron

(Figure X(a)), similar in shape to the electron jack seen in chromium but not topologically equivalent to it. Part of band 3 forms a hole ellipsoid surrounding N (Figure X(b)) as in chromium but containing a larger fraction of the Brillouin zone volume. The remainder of band 3 forms the "jungle-gym". This consists of open tubes along [100] directions which interconnect with those in neighboring Brillouin zones.

Cross-sections of these Fermi surface features in a (001) plane are shown in Figure XI. A comparison of the areas and dimensions of the features with the calculations of Boyer, et al.[35] and with the available experimental data is presented in Table V. Unlike chromium, the "nesting" was quite weak, indicating a lack of observable Kohn anomalies in any neutron scattering experiments for vanadium. Although no closed orbit has been observed around the octahedron at Γ, Parker and Halloran[74] have reported the orbit around the arm of the jungle-gym from measurements of magnetothermal oscillations. The ellipsoids around N have been examined by them as well as by Phillips[75] using the de Haas-van Alphen effect. These investigators probed the cross-sectional areas (orbits) of these ellipsoids in many orientations. On the whole, the areas we calculate are about 15 to 20 percent larger than the measured values while Boyer, et al. obtain values consistently too small.

Although Wakoh and Yamashita do not give numbers for the areas, their results also appear to be larger than the experimental results (for the KSG potential). Thus we assume that the difference between our areas and those of Reference 35 is due to differences in band structure rather than other reasons (such as the method of locating the Fermi surface). The most probable reasons are either the muffin-tin potential used in their APW calculation or the degree of self-consistency they achieved.

The effective mass ratios have also been computed for vanadium and are listed in Table VI. Also displayed are the results of the calculations of Papaconstantopoulos, et al.[34] and Boyer, et.al.[35] and the measurements of Parker and Halloran[74] and Phillips.[75]

The general agreement with the experimental Fermi surface is reasonable but the dimensions of features, especially small ones, are not predicted accurately. Calculations on many materials have noted this problem, but nowhere is it more acute than for copper. The radii of the belly orbit and the neck at the L point are known with great precision. Even the latest first-principles calculations of Bagayoko, et. al.[51] and Janak, et. al.[52] obtain a neck radius that is nearly 20 percent too large. Janak, et.al. found that neither gradient corrections nor relativistic corrections produced much better results. Although they were able to match the dimensions,

they had to use a value of α (0.77) that does not correspond to either of the theoretical values. It has been suggested[76] that local potentials are simply not able to produce good Fermi surfaces. Investigations of the non-local contributions to the energy by Wang and Rasolt[76] produced results as accurate as the best results of Janak, et al.

CHAPTER IV

CALCULATED QUANTITIES

This chapter, consisting of three sections, will examine quantities which are derivable from the energy band structure. Section A discusses the X-ray form factors which are simply related to the Fourier components of the charge density. In the following section (B), the Compton profiles are examined. In order to make the comparison with experiment easier, the spherical average was computed from the directional profiles and the anisotropy of the profiles is also discussed. Finally, the optical conductivity appears in Section C along with the transitions most likely to be responsible for each major structure and the electron energy-loss spectrum.

A. X-Ray Form Factors

The X-ray scattering form factors are the scaled intensities of the various orders of diffracted X-rays. Theoretically, the form factors are proportional to the Fourier coefficients of the charge density evaluated at reciprocal lattice vectors. If we denote N as the number of electrons in the system (N = 24 for chromium and N = 23 for vanadium) and $\rho_o = \rho(\vec{K}=0)$, then the form factors are given by the expression

$$F(\vec{K}) = N\ \rho(\vec{K})/\rho_o$$

In the calculational scheme we use, the Fourier coefficients are a required part of the self-consistency routine and are written at the end of each iteration. Thus, it is a trivial matter to compute $F(\vec{K})$ for the first few smallest-magnitude reciprocal lattice vectors. In addition, the ratios F(330)/F(411) and F(442)/F(600) are important because these pairs of reciprocal lattice vectors have the same magnitude but different orientations in space providing a measure of the asphericity of the charge density.

Table VI contains the form factors for chromium. The KSG and VBH exchange potentials agree to better than 1 percent so only the VBH results are shown. Also listed are the computed form factors of Rath and Callaway[33] and of Wakoh and Yamashita[77] and the various experiments[12-14] along with their associated uncertainties (when known). The agreement is reasonable, in view of the amount of disagreement among the experiments. Note, however, that Hosoya[15] observed a decrease in F(110) (and presumably all other form factors) with time and concluded that Cooper's result[13] was probably too low. Our results for both asphericity ratios agree with the experimental uncertainty.

The form factors for vanadium are listed in Table VII. The amount of experimental data available for comparison is limited. However, Terasaki, et. al.[26] has reported results for F(110) and F(200) which are reasonably close to our calculated form factors. The asphericity ratio F(330)/F(411) has been measured by Weiss and DeMarco[10] and Diane and Mazzone.[12] Their results are 1.012 and 1.0085 respectively which are much larger than the calculated values (1.0039 for our calculation and 1.0015 from Wakoh and Yamashita[77]).

B. Compton Profiles

The differential cross-section for Compton scattering of X-rays by electrons is proportional[78] to the Compton profile

$$J_{\hat{k}}(q) = \frac{\Omega}{(2\pi)^3} \int \rho(\vec{p})\, \delta(q - \vec{p}\cdot\hat{k})\, d\vec{p}$$

where q is the component of momentum along $\hat{k}$. The electron momentum density $\rho(\vec{p})$ is given by

$$\rho(\vec{p}) = \sum_{n\vec{g}} |\psi_n(\vec{g},\vec{p})|^2$$

where $\psi_n(\vec{g},\vec{p})$ is the wavefunction in momentum space (the Fourier transform of the real-space wavefunction $\psi_n(\vec{g},\vec{r})$).

This result was obtained in the impulse approximation in which the energy transferred to an electron during the collision is much larger than that electron's binding energy. The profiles obey the normalization condition

$$\int_0^\infty J_k^\wedge(q)dq = n_e$$

where n_e is the number of electrons per atom (or the number per shell if $J_k^\wedge(q)$ is decomposed on a shell-by-shell basis).

In the LCGO formalism, this calculation requires the Fourier transforms of the Gaussian basis functions evaluated at a large number of reciprocal lattice vectors. The rate of convergence is determined primarily by the exponents of these Gaussians[79]: band states which have small exponents converge rapidly while core states with large exponents converge very slowly. Approximately 2000 independent reciprocal lattice vectors provided profiles that were converged sufficiently (to about 0.01 percent) for the band states, but not for the core states (1s, 2s, 2p, 3s and 3p). (A more complete discussion of the procedures used here may be found in Reference 79.) Hartree-Fock Compton profiles are available (Weiss, et al.[80]) for both chromium and vanadium (free atoms) decomposed by band for states whose binding energy is less than 1500 eV. Although this excludes the 1s state

for the 3d metals, the 1s contribution to the total profile is small. We have subtracted the core contributions (based on these Hartree-Fock results) from the experimental profiles (when necessary) to extract that portion due to band electrons alone.

Tables VIII and IX contain numerical values for the calculated Compton profiles of (respectively) chromium and vanadium in the three principal directions: (100), (110) and (111). Also listed are the spherical averages for the sake of comparison with the results obtained using polycrystalline samples. Our calculated average Compton profile for chromium agrees reasonably well with the results of Paakkari, Manninen and Berggren[23] (see Figure XII) although it tends to underestimate the experimental results over the entire range of q values. This underestimation is attributed to the neglect of the 1s contribution, which, although small, has a very flat long-range behavior. The difference between the (111) and (100) directional profiles is compared in Figure XIII to the anisotropy measured by Weiss.[24] The anisotropy is rather small over most of the range but the trends are predicted correctly and the magnitudes are reasonably good. In Figure XIV, our spherical average for vanadium has been plotted along with the profile measured by Phillips.[25] The agreement is quite good although the experiment gives a larger profile than our calculation

at large q values. Not shown in Figure XIV is the profile reported by Manninen and Paakkari[22] which is in very good agreement with that of Phillips. The anisotropy of the Compton profiles for vanadium are shown in Figure XV for the same pair of directions as was displayed for chromium ((111) - (100)). Measurements of all three anisotropies have been reported by Terasaki, et. al.[26] but their results are plotted in figures too small to enable us to extract any useful information. The profiles of vanadium have also been calculated by Wakoh, Kubo, and Yamashita.[81] For small q values ($q < 0.5$), the agreement with our results is excellent, generally being about 1 to 2 percent. But for larger values of q, our results are consistently higher than theirs. We are inclined to believe that their APW wavefunctions are not sufficiently converged.

C. Optical Conductivity

The frequency-dependent interband optical conductivity in the sharp-band limit (infinite relaxation time) is given by the standard formula[82]

$$\sigma(\omega) = (2\pi e^2/3m^2\omega) \sum_{n\ell} \int d\vec{k}/(2\pi)^3 |\vec{p}_{\ell n}(\vec{k})|^2 f_\ell(\vec{k})$$

$$(1 - f_n(\vec{k}))\ \delta(\omega_{n\ell}(\vec{k}) - \omega) \qquad (9)$$

where $f_\ell(\vec{k})$ and $f_n(\vec{k})$ are the Fermi occupation probabilities for the states $|\ell\vec{k}>$ and $|n\vec{k}>$ and

$$\omega_{n\ell}(\vec{k}) = (E_n(\vec{k}) - E_\ell(\vec{k}))/\hbar$$

The term $f_\ell(\vec{k})\ (1 - f_n(\vec{k}))$ prevents the inclusion of transitions between two occupied or two unoccupied states. Energy conservation is assured by the delta function and the momentum matrix elements are

$$\vec{P}_{\ell n}(\vec{k}) = <\ell\vec{k}|-i\hbar\vec{\nabla}|n\vec{k}>$$

The use of Gaussian functions as the basis set allows analytic evaluation of these matrix elements and also allows us to retain their $\vec{k}$-dependence. Thus, we are not forced into the rather drastic assumption that the matrix element is constant throughout the Brillouin zone which provides results of questionable quality. In such an approximation,

$$\sigma(\omega) \ \alpha \ \sum_{n\ell} G_{n\ell}(\omega)$$

where $G_{n\ell}(\omega)$ is the <u>joint density of states</u> given by

$$G_{n\ell}(\omega) = \frac{\Omega}{(2\pi)^3} \int \delta(\omega_{n\ell}(\vec{k}) - \omega)\ d\vec{k}$$

The same form of tetrahedral integration used to compute the density of states is applied here with the matrix elements linearly interpolated within each tetrahedron.

Because the experiments can only measure the total conductivity, some attempt must be made to add the intra-band contribution to our results. This is done in the Drude approximation which gives a term of the form

$$\sigma_D(\omega) = \sigma_o/(1 + \omega^2 \tau_D^2)$$

The Drude constants were determined by an empirical fit by Lenham and Treherne[83] to available experimental data in the near infrared. The total conductivity thus obtained must satisfy the usual sum rule

$$\int_o^\infty \sigma(\omega)\, d\omega = \pi N e^2/2m$$

where m is the free electron mass and N is the number of electrons per unit volume. The obvious lack of sharp structure in the experimental curves has been attributed to a substantial lifetime broadening of the excited states of the solid. This lifetime broadening has an estimated value of 0.2 eV (for chromium) based upon a crude line-shape analysis of thermoreflectance data.[84] However, since there is no solid evidence for any particular value of broadening beyond this order-of-magnitude estimate,

we examine a range of factors from 0.05 eV to 1.0 eV. This broadening is included by averaging our calculated conductivity over a Lorentzian distribution. The value 0.5 eV seemed to give the best results for both chromium and vanadium when compared to the experimental curves. The fact that this lifetime differs from the Drude value is of some concern and, in fact, this simple method of smoothing the data may not be consistent with the above-mentioned sum rule.

When the experimental maxima are compared to the calculated values, there is often a considerable mismatch in position which gets worse as the energy gets higher. Because this effect appears in virtually every ab initio calculation using any kind of local exchange approximation, it has been associated with the local density approximation (LDA) itself. As the current state of computation in band structure does not permit reasonable use of a non-local exchange potential, some method of correcting the LDA must be used. One such technique is the introduction of an electron self-energy correction which has the form

$$\tilde{E}_n(\vec{k}) = E_n(\vec{k}) + \lambda_n(\vec{k})\,(E_n(\vec{k}) - Ef) \qquad (10)$$

(see Appendix B for more information). Here $\tilde{E}_n(\vec{k})$ is the corrected energy for band n whose original

(uncorrected) energy was $E_n(\vec{k})$ and $\lambda_n(\vec{k})$ is the diagonal matrix element of a correlation matrix. In order to simplify the calculations, Janak, Williams and Moruzzi[85] first assumed that the matrix element is independent of $\vec{k}$ and n. Thus, they reduce equation (10) to

$$\tilde{E}_n(\vec{k}) = E_n(\vec{k}) + \lambda(E_n(\vec{k}) - Ef) \qquad (11)$$

Hence, each band energy is scaled by a factor proportional to the difference between that energy and the Fermi energy. Then Janak, et al. carried this scaling through to the calculation of the dielectric function

$$\tilde{\varepsilon}(\omega) = 1/(1 + \lambda)\,\varepsilon(\omega/(1 + \lambda))$$

and obtained good agreement with the experimental results for copper using $\lambda = 0.08$. The corresponding formula for the scaled optical conductivity

$$\tilde{\sigma}(\omega) = 1/(1 + \lambda)^2\,\sigma(\omega/(1 + \lambda))$$

was used with a reasonable degree of success in a study[86] of the conductivities of iron ($\lambda = -0.1$) and nickel ($\lambda = -0.12$). We chose for λ that value which brings an arbitrarily chosen theoretical feature into coincidence with the position determined by the experiments. The plus

(minus) sign on λ is decided on the basis that the computed conductivity needs to be expanded (contracted). Apart from an empirical correction, no physical significance is attached to λ in this work.

The calculated optical conductivity of chromium is plotted in Figure XV along with the experimental results of Nestell and Christy[20] and Ganin, et al.[18] The uncorrected interband portion (as computed from equation (9)) is labelled "curve A". Table XII contains a listing of both the interband optical conductivity and the <u>total</u> joint density of states

$$G(E) = \sum_{n\ell} G_{n\ell}(E)$$

as a function of energy. The result shown in curve B has been smoothed with a broadening factor of 0.5 eV and a Drude term has been added (using $\sigma_o = 7.0 \times 10^{15}$ sec^{-1} and $\tau_D = 7.27 \times 10^{-15}$ sec). Finally, the self-energy correction (curve C) is included with $\lambda = -0.1$ (the same value obtained for iron). This value caused our calculated peak at 6.3 eV to coincide with the 5.9 eV peak in the experimental data. Unfortunately, the correction to the <u>position</u> of the main peak was not enough while its <u>magnitude</u> was made too large. This indicates that the self-energy correction is not adequate when included in this simple way.

The contributions to the (interband) conductivity were not separated by band in order to simplify the computer programs and to minimize the amount of computer time used. As a consequence, it is not possible for us to uniquely assign specific transitions to a particular peak. However, by using symmetry rules and energy differences, we can make probable assignments. The $\Delta_5 \rightarrow \Delta_2'$ transition with a threshold of 1 eV is probably the main contributor to our 1.2 eV peak which is close to a peak reported in thermoreflectance measurements.[21] The 1.9 eV peak is presumably due to $\Delta_5 \rightarrow \Delta_1$ and $\Sigma_1 \rightarrow \Sigma_4$ transitions. Thermoreflectance data also find structure in this region. The main peak and the peak near 6.3 eV are the result of a large number of transitions from an extremely large region of the Brillouin zone.

Figure XVI contains plots of the calculated optical conductivities of vanadium along with the experimental results of Nestell and Christy.[20] Curve A is the uncorrected interband optical conductivity and curve B is the smoothed result (with 0.5 eV of broadening) to which a Drude term (with $\sigma_o = 4.8 \times 10^{15}$ sec^{-1} and $\tau_D = 5.47 \times 10^{-15}$ sec) has been added. The interband portion of the conductivity and the total joint density of states are listed in Table XIII. The self-energy correction factor ($\lambda = -0.08$) that brought the computed 6.3 eV peak into coincidence with the 6.0 eV experimental peak is labelled "curve C".

The peak near 2 eV can be tentatively assigned to a $\Sigma_1 \rightarrow \Sigma_1$ transition and the 6.25 eV peak is probably a $\Lambda_1 \rightarrow \Lambda_3$ transition. As in the chromium case, the transitions contributing to the main peak (3.3 eV) are too varied and from too large a region of the Brillouin zone to enumerate. However, Rosei, et al.[84] have used thermoreflectance measurements to deduce the threshold energies of three important transitions. Their results are listed in Table XI along with our energy differences and those of three other calculations.[87,88]

The complex dielectric function is related to the (complex) optical conductivity by the formula

$$\varepsilon = 1 + i\sigma/\omega \tag{12}$$

It is known that the maximum of the energy loss function

$$\mathrm{Im}(-1/\varepsilon) = \varepsilon_2/(\varepsilon_1^2 + \varepsilon_2^2)$$

occurs at the plasma frequency. Here, ε_1 and ε_2 are the real and imaginary parts (respectively) of the dielectric function. If we substitute equation (12) into this formula, the loss function becomes

$$\mathrm{Im}(-1/\varepsilon) = \omega\,\sigma_2/((\omega + \sigma_1)^2 + \sigma_2^2)$$

Hence, we need both the real and the imaginary parts of the conductivity whereas we have only calculated the real part. However, the imaginary part can be obtained by the use of the Kramers-Kronig relation

$$\sigma_2(\omega) = -\frac{2\omega}{\pi} P \int_0^\infty \sigma_1(\nu)\, d\nu/(\nu^2 - \omega^2)$$

The results for chromium are presented in Figure XVIII in the sharp limit (solid line) and with the 0.5 eV lifetime broadening factor (dash-dot line). The agreement is very good for energies below 5 eV but the peak seen in the theoretical curve near 6.3 eV is not observed in the experimental results (Nestell and Christy[20] - dashed line, Lynch[89] - dotted line). Programming restrictions prevented accurate determination of the real part (and hence the imaginary part) of the optical conductivity for energies much greater than 6 eV while the interesting structure occurs near 9 eV.[89] The recent calculations of Kubo and Wakoh[93] produced results very close to ours.

CHAPTER V

CONCLUSION

Self-consistent energy bands for paramagnetic chromium and vanadium have been generated using the LCGO method. Two local exchange potentials (the familiar Kohn-Sham-Gaspar potential and an exchange-correlation potential due to von Barth and Hedin) were compared for chromium while the Kohn-Sham-Gaspar exchange alone was used for vanadium. The calculations are current state-of-the-art and produced bands converged to better than 0.0001 Rydberg. The self-consistent energies and wavefunctions were generated at enough points (506 in the irreducible wedge of the Brillouin zone) to enable accurate numerical evaluation of all required integrals.

The comparison of the two exchange potentials was rather confusing. Although the VBH bands are narrower than the KSG bands and hence closer to the experimental band widths, the difference is only 0.1 eV which is less than 20 percent of the change needed to match the experimental findings. For some quantities, such as the X-ray form factors, the two results are almost indistinguishable. Neither potential gave consistently better Fermi surface dimensions but the VBH exchange did come closer to the experimental effective masses. Thus, we judge the VBH exchange-correlation potential to be better (marginally) than the KSG exchange for paramagnetic

systems. This is roughly the same conclusion reached in the ferromagnetic studies.

The energy bands agree well with other current self-consistent calculations. Unfortunately, the question of the ordering of the states at the N point for chromium still remains unanswered as the position of the p-like state N_1' is very sensitive to the potential used in the calculation. The bands remain wider (about 10 percent for chromium and 6 percent for vanadium) than values reported in photo- and X-ray emission experiments. As expected, the densities of states are all nearly identical and dominated by two large peaks separated by a shallow minimum. The Fermi energy lies near the bottom of this minimum for chromium and near the top of the lower-energy peak for vanadium. When comparing the electronic specific heat to experiments, the phonon renormalization factors are near 1.8 for chromium and 2.3 for vanadium. Thus, the electron-phonon interaction is much stronger in vanadium than in chromium. The phonon renormalization factor for the antiferromagnetic state of chromium is estimated to be 1.3 implying a weakening of the electron-phonon interaction in this state.

Although the essential features of the Fermi surface are present, the dimensions and areas, especially of small portions, are not accurately predicted. The reason for this discrepancy has been attributed by other authors

to the neglect of the non-local nature of exchange and correlation and the results of this work cannot dispute this claim.

The computed X-ray form factors did not lie within the experimental uncertainties but the amount of disagreement between the experiments themselves is also greater than the individual uncertainties. The Compton profiles do generally agree with the measured valued if the spherical average is used in the comparison, although the computed profile tends to lie above the measured values at large q (q > 4 a.u.). The directional differences reproduced the overall behavior of the experimental results but the magnitudes did not match very well. The lack of structure in the experimental optical conductivities are interpreted as the result of rather large lifetime broadening. We included an empircally chosen broadening factor (0.5 eV) which seemed to reproduce the observed smoothing reasonably well. A self-energy correction (λ) allowed us to shift the positions of the major peaks to correspond with the experimental positions using a value of -0.1 for chromium and -0.08 for vanadium.

Several improvements to the computer codes and to the method itself could be made. The first is that a <u>contracted</u> basis set could be used. It should be possible to contract to 6 or 7 s-like and 4 or 5 p-like states without sacrificing accuracy. The resulting matrix would be about 2/3 as large as the current matrix and should

thus run in 1/2 to 1/3 of the time required for the current programs. However, the effect of such a contraction upon calculated properties must be investigated carefully before abandoning the complete basis. One of the ideal improvements would be the inclusion of a non-local correction to the exchange potential. The gradient expansions that have been used to date have not produced a satisfactory degree of correction. Unfortunately, no such potential exists in a form suitable for current state-of-the-art tight-binding calculations.

REFERENCES

1. W. Kohn and L. J. Sham, Phys. Rev. 140, A1133 (1965).

2. R. Gaspar, Acta Phys. Acad. Sci. Hung. 3, 263 (1954).

3. U. von Barth and L. Hedin, J. Phys. C 5, 1629 (1972).

4. R. P. Gupta and S. K. Sinha, Phys. Rev. B 3, 2401 (1971); see also K. H. Oh, B. N. Harmon, S. H. Liu and S. K. Sinha, Phys. Rev. B 14, 1283 (1976).

5. W. M. Lomer, Proc. Phys. Soc. London 80, 489 (1962); 84, 327 (1964).

6. W. M. Shaw and L. D. Muhlestein, Phys. Rev. B 4, 969 (1971).

7. L. D. Muhlestein, E. Gurmen and R. M. Cunningham, in "Inelastic Scattering of Neutrons" (IAEA, Grenoble, 1972), p. 53.

8. L. D. Muhlestein, E. Gurman and R. M. Cunningham, in "Proceedings of the 18th Annual Conference on Magnetism and Magnetic Materials" (A.I.P., New York, 1972).

9. O. Terasaki, Y. Uchida and D. Watanabe, J. Phys. Soc. Japan 39, 1277 (1975).

10. R. J. Weiss and J. J. de Marco, Phys. Rev. 140, A1223 (1965).

11. M. Diana and G. Mazzone, Philos. Mag. 32, 1227 (1975).

12. M. Diana and G. Mazzone, Phys. Rev. B 5, 3832 (1972).

13. M. J. Cooper, Philos. Mag. 7, 2059 (1962); 10, 177 (1964).

14. M. Fujimoto, O. Terasaki and D. Watanabe, Phys. Lett. 41A, 159 (1972).

15. S. Hosoya, J. Phys. Soc. Japan 19, 235 (1964).

16. S. K. Sinha, G. R. Kline, C. Stassis and N. Chesser, Phys. Rev. B 15, 1415 (1977).

17. A. S. Barker, Jr. and J. A. Ditzenberger, Phys. Rev. B 1, 4378 (1970).

18. G. V. Ganin, M. M. Kirillova, I. V. Nomerovannaya and V. P. Shirokovskiy, Fiz. Metal. Metallov. 43, 907 (1977).

19. P. B. Johnson and R. W. Christy, Phys. Rev. 139, 5056 (1974).

20. J. E. Nestell, Jr. and R. W. Christy, Phys. Rev. B 21, 3173 (1980).

21. J. H. Weaver, D. W. Lynch, C. H. Culp and R. Rosei, Phys. Rev. B 14, 459 (1976).

22. S. Manninen and T. Paakkari, Phys. Fennica 9, 129 (1974).

23. T. Paakkari, S. Manninen and K. F. Berggren, Phys. Fennica 10, 207 (1975).

24. R. J. Weiss, Philos. Mag. 27, 1461 (1973).

25. W. C. Phillips, Phys. Rev. B 7, 1047 (1973).

26. O. Terasaki, T. Fukamachi, S. Hoysoya and D. Watanabe, Phys. Lett. A 43, 123 (1973).

27. M. O. Steinitz, E. Fawcett, C. E. Burlson, J. A. Schaefer, L. O. Frishman and J. A. Marcus, Phys. Rev. B 5, 3675 (1972).

28. R. Griessen and E. Fawcett, J. Phys. F 7, 2141 (1977).

29. A. J. Arko, J. A. Marcus and W. A. Reed, Phys. Rev. 176, 671 (1968).

30. J. E. Graebner and J. A. Marcus, Phys. Rev. 175, 659 (1968).

31. S. Kotani and N. Mori, Solid State Commun. 27, 1013 (1978).

32. For example, see C. N. Berglund and W. E. Spicer, Phys. Rev. 136, A1030 (1964); 136, A1044 (1964).

33. J. Rath and J. Callaway, Phys. Rev. B 8, 5398 (1973).

34. D. Papaconstantopoulos, J. R. Anderson and J. W. McCaffrey, Phys. Rev. B 5, 1214 (1972).

35. L. D. Boyer, D. Papaconstantopoulos and B. M. Klein, Phys. Rev. B 15, 3685 (1977).

36. A. Asano and J. Yamashita, J. Phys. Soc. Japan 23, 714 (1967).

37. S. Wakoh and J. Yamashita, J. Phys. Soc. Japan 35, 1394 (1973).

38. M. Yasui, E. Hayashi and M. Shimizu, J. Phys. Soc. Japan 29, 1446 (1970).

39. H. L. Skriver, to be published.

40. F. Bloch, Zeit. Physik 52, 555 (1928).

41. E. E. Lafon and C. C. Lin, Phys. Rev. 152, 579 (1966).

42. R. C. Chaney and F. Dorman, Inter. J. Quan. Chem. 8, 465 (1974).

43. C. S. Wang and J. Callaway, Comp. Phys. Commun. 14, 327 (1978).

44. J. C. Slater, Phys. Rev. 81, 385 (1951).

45. A. K. Rajagopal and J. Callaway, Phys. Rev. B 7, 1912 (1973).

46. J. Callaway and C. S. Wang, Phys. Rev. B 16, 2095 (1977).

47. C. S. Wang and J. Callaway, Phys. Rev. B 15, 298 (1977).

48. L. Hedin and B. I. Lundquist, J. Phys. C 4, 2064 (1971).

49. A. K. Rajagopal, S. P. Singhal and J. Kimball, unpublished; see A. K. Rajagopal in "Advances in Chemical Physics", edited by G. T. Prigogine and S. A. Rice (Wiley, New York, 1979), Volume 41.

50. S. P. Singhal and D. Bagayoko, private communication.

51. D. Bagayoko, D. G. Laurent, S. P. Singhal and J. Callaway, Phys. Lett. 76A, 187 (1980).

52. J. F. Janak, A. R. Williams and V. L. Moruzzi, Phys. Rev. B 6, 4367 (1972).

53. M. I. Chodorow, Ph. D. thesis (M.I.T., 1939), cited in Reference 52, but otherwise unpublished.

54. J. L. Fry, N. E. Brener, J. L. Thompson and P. H. Dickinson, Phys. Rev. B 21, 384 (1980).

55. J. Callaway and J. L. Fry in "Computational Methods in Band Theory", edited by P. M. Marcus, J. F. Janak and A. R. Williams (Plenum, New York, 1972), p. 512.

56. A. J. H. Wachters, J. Chem. Phys. 52, 1033 (1970).

57. G. Gilat and L. J. Raubenheimer, Phys. Rev. 144, 390 (1966).

58. J. D. Connolly, Inter. J. Quan. Chem. 25, 257 (1968).

59. L. F. Mattheiss, Phys. Rev. 139, A1893 (1965).

60. L. I. Johansson, L. G. Peterson, K. F. Berggren and J. W. Allen, Phys. Rev. B 22, 3294 (1980).

61. A. J. McAllister, J. P. Cuthill, R. C. Dobbyn, M. L. Williams and R. E. Watson, Phys. Rev. B 12, 2973 (1975).

62. J. R. Anderson, J. W. McCaffrey and D. Papaconstantopoulos, Solid State Commun. 7, 1493 (1969).

63. T. M. Hattox, J. B. Conklin, J. C. Slater and S. B. Trickey, Jr., Phys. Chem. Solids 34, 1627 (1973).

64. L. F. Mattheiss, Phys. Rev. B 1, 373 (1970).

65. The value $\alpha = 0.71556$ duplicated the Hartree-Fock total energy when used in a Hartree-Fock-Slater calculation. See K. Schwarz, Phys. Rev. B 5, 2466 (1972) and Theor. Chim. Acta 34, 225 (1974).

66. D. E. Eastman, Solid State Commun. 7, 1697 (1969).

67. D. W. Fischer, J. Applied Phys. 40, 4151 (1969).

68. C. F. Hague and C. Bonnelle in "Band Structure Spectroscopy of Metals and Alloys", edited by D. J. Fabian and L. M. Watson (Academic, New York, 1973), p. 25.

69. P. Heiniger, E. Bucher and J. Mueller, Phys. Kondens Materie 5, 243 (1966).

70. For example, see J. Callaway, Quantum Theory of the Solid State, (Academic, New York, 1978), p. 594.

71. J. L. Fry, N. E. Brener, D. G. Laurent and J. Callaway, presented at the Conference on Magnetism and Magnetic Materials, Dallas, Texas, June, 1980.

72. W. Kohn, Phys. Rev. Lett. 2, 393 (1959).

73. L. M. Roth, H. J. Zeiger and T. A. Kaplan, Phys. Rev. 149, 519 (1966).

74. R. D. Parker and M. Halloran, Phys. Rev. B 9, 4130 (1974).

75. R. A. Phillips, Phys. Lett. A 36, 361 (1971).

76. J. S. Y. Wang and M. Rasolt, Phys. Rev. B 15, 3714 (1975).

77. S. Wakoh and J. Yamashita, J. Phys. Soc. Japan 30, 422 (1971).

78. The double differential cross-section is given by $d^2\sigma/d\omega d\Omega = (e^2/mc^2)^2(\vec{\epsilon}_1\cdot\vec{\epsilon}_2)^2(\omega_2/\omega_1)\ m/|\vec{k}|\ J_{\hat{k}}(q)/\omega$. For example, see P. M. Platzman and N. Tjoar, Phys. Rev. 139, A410 (1965).

79. J. Rath, C. S. Wang, R. A. Tawil and J. Callaway, Phys. Rev. B 11, 5139 (1973).

80. R. J. Weiss, A. Harvey and W. C. Phillips, Philos. Mag. 17, 241 (1968).

81. S. Wakoh, Y. Kubo and J. Yamashita, J. Phys. Soc. Japan 40, 1043 (1976).

82. For example, see W. Y. Ching and J. Callaway, Phys. Rev. B 11, 1324 (1975).

83. A. P. Lenham and D. M. Treherne in "Optical Properties and Electronic Structure of Metals and Alloys", edited by F. Abeles (North-Holland, Amsterdam, 1966), p. 196.

84. R. Rosei, E. Colavita, A. Franciosi, J. H. Weaver, and D. T. Peterson, Phys. Rev. B 21, 3152 (1980).

85. J. F. Janak, A. R. Williams and V. L. Moruzzi, Phys. Rev. B 11, 1522 (1976).

86. D. G. Laurent, J. Callaway and C. S. Wang, Phys. Rev. B 20, 1134 (1979).

87. J. F. Alward, C. Y. Fong and C. Guha Sridhar, Phys. Rev. B 18, 5438 (1978).

88. A personal communication from D. D. Koelling is reported by the authors of Reference 84.

89. D. W. Lynch, private communication.

90. P. Hohenberg and W. Kohn, Phys. Rev. 136, B864 (1964).

91. L. J. Sham and W. Kohn, Phys. Rev. 145, 561 (1966).

92. For example, see S. H. Vosko, L. Wilk and M. Nusair, Canadian Jour. Phys. 58, 1200 (1980).

93. Y. Kubo and S. Wakoh, J. Phys. Soc. Japan 50, 835 (1981).

TABLE I

Absolute Energy Differences Between the KSG and the VBH Exchange Potentials

Energy	KSG	VBH	Difference	Symmetry
E_f	-0.42776	-0.58058	0.1528	---
Γ_1	-0.99625	-1.14038	0.1441	1
Γ'_{25}	-0.49403	-0.64799	0.1540	xy,yz,zx
Γ_{12}	-0.35089	-0.50399	0.1531	$x^2-y^2, z^2-1/3$
N_1	-0.74835	-0.89715	0.1488	$1, xy, z^2-1/3$
N_2	-0.60396	-0.75649	0.1525	z(x-y)
N'_1	-0.35879	-0.50338	0.1446	x+y
N_1	-0.34998	-0.50382	0.1538	$xy, z^2-1/3$
N_4	-0.32743	-0.48100	0.1536	x^2-y^2
N_3	-0.22483	-0.38151	0.1567	z(x+y)
P_4	-0.59812	-0.74884	0.1507	x^2-y^2
P_3	-0.32335	-0.47697	0.1536	x,y,z,xy,yz,xz
H_{12}	-0.74055	-0.88939	0.1488	$x^2-y^2, z^2-1/3$
H'_{25}	-0.25290	-0.40925	0.1564	xy,yz,zx
H_{15}	0.32386	0.17867	0.1452	x,y,z

TABLE II

Energy Differences for Selected States of Chromium

States	Present (KSG)	(VBH)	Ref. 54	Ref. 33	Ref. 36	Ref. 4	Ref. 38
$E_f-\Gamma_1$	.5678	.5599	.7143	.536	.5175	.624	.500
$\Gamma_{12}-\Gamma_1$	.6454	.6364	.8210	.6102	.5785	.709	.569
$\Gamma_{12}-\Gamma_{25'}$	.1431	.1440	.1715	.1590	.1332	.136	.145
$\Gamma_{25'}-\Gamma_1$	.5022	.4924	.6495	.4513	.4453	.573	.424
$H_{25'}-H_{12}$	.4877	.4801	.6620	.4812	.4848	.523	.467
$H_{15}-\Gamma_1$	1.3201	1.3201	1.3723	1.2644	---	1.330	1.097
$H_{25'}-\Gamma_{25'}$	.2411	.2387	.3166	.2670	.2341	.238	.298
$\Gamma_{12}-H_{12}$	.397	.3854	.5168	.3730	.3840	.421	.314
P_3-P_4	.2748	.2719	.3813	.2670	.2505	.300	.227
N_2-N_1	.1444	.1407	.2089	.1234	.1327	.170	.109
N_3-N_1	.5235	.5156	.7132	.5302	.5025	.558	.498
$N_4-N_1(2)$	.0226	.0228	.0343	.0211	.0201	.024	-.011
$N_{1'}-N_4$	-.0314	-.0224	-.1876	.0115	.0531	-.109	.074
$N_3-N_{1'}$	.1340	.1219	.3303	.1087	.0498	.215	.069

TABLE III

Energy Differences for Selected States of Vanadium

States	Present	Ref. 38	Ref. 34
$E_f-\Gamma_1$	.4701	.440	.497
$\Gamma_{12}-\Gamma_1$	.6410	.440	--
$\Gamma_{12}-\Gamma_{25'}$	.1410	.148	--
$\Gamma_{25'}-\Gamma_1$	.5000	.454	.543
$H_{25'}-H_{12}$	.4757	.476	.535
$H_{15}-\Gamma_1$	1.1893	1.012	--
$H_{25'}-\Gamma_1$	.7345	.758	.791
$H_{25'}-\Gamma_{25'}$	.2345	.304	--
$\Gamma_{12}-H_{12}$	.3822	.320	--
P_3-P_4	.2805	.241	--
N_2-N_1	.1473	.121	--
N_3-N_1	.5173	.513	--
$N_4-N_1(2)$	.0244	-.014	--
$N_{1'}-N_4$	-.0876	.002	--
$N_3-N_{1'}$	.1843	.140	--

TABLE IV

Analysis of Kohn Anomalies for Chromium

Fermi Surface Feature	Direction of Phonon Anomaly	Exp. Value	Theoretical Value (KSG)	Theoretical Value (VBH)
$\overline{\Gamma P}$ Extremum of Electron Jack	Along $\overline{\Gamma P}$	.25(111)	.27(111)	.26(111)
$\overline{\Gamma H}$ Extremum of Electron Jack	Along $\overline{\Gamma H}$ near H	.85(001)	.82(001)	.83(001)
Nesting of Jack Body and Hole at N	Along $\overline{\Gamma N}$	.46(011)	.42(011)	.42(011)
Nesting of Ball and Holes at N along (111)	Near P	.54(111)	.54(111)	.54(111)
Nesting of Jack Body and Hole at H in (111) direction	Along $\overline{PH}$ near H	.98(111)	.98(111)	.99(111)
Nesting of Jack Body and Hole at H in (001) direction	Spin-Density wave	.96(001)	.95(001)	.96(001)

TABLE V

Chromium Fermi Surface Data

Dimensions of Holes at N(in $\mathring{A}^{-1}$)

Direction	Experiment	KSG Result	VBH Result
$\overline{NH}$	.173	.186	.185
$\overline{N\Gamma}$	.234	.304	.311
$\overline{NP}$	.268	.316	.324

De Haas-van Alphen Frequencies (in megaGauss)

Plane	Experiment(*)	KSG Result	VBH Result
ΓNH	13.3	18.6	18.9
ΓNP	20.6	31.6	33.2
HNP	15.3	19.3	19.7

Effective Mass Ratios for the Holes at N

Plane	Experiment	KSG Result	VBH Result
ΓNH	.27-.43	.45	.42
ΓNP		.53	.21
HNP		.45	.30

Dimensions of Ball at X (in $\mathring{A}^{-1}$)

Direction	Experiment	KSG Result	VBH Result
$\overline{\Gamma H}$	.26	.30	.32
$\overline{XN}$	.25	.30	.30

(*) Computed from the dimension given Ref. 30.

TABLE VI

Vanadium Fermi Surface Data

Dimensions of Holes at N (in $\mathring{A}^{-1}$)

Direction	Present	Ref.74	Ref.75	Ref.35	Ref.34
$\overline{NH}$	.361	.365	.366	---	---
$\overline{N\Gamma}$	.504	.441	.441	---	---
$\overline{NP}$	.530	.463	.465	---	---

de Haas-van Alphen Frequencies (in megaGauss)

Plane	Present	Ref.74	Ref.75	Ref.35	Ref.34
ΓNH	59.9	52.9	52.6	41.9	44.9
ΓNP	87.9	67.1	67.1	56.6	59.5
HNP	62.9	55.6	55.7	55.5	46.5

Effective Mass Ratios for the Holes at N

Plane	Present	Ref.74	Ref.75	Ref.35	Ref.34
ΓNH	1.1	1.77	---	.72	.86
ΓNP	1.7	---	---	.91	1.3
HNP	.9	2.20	---	.88	.92

TABLE VII

X-ray Form Factors of Chromium

$\frac{a}{2\pi}\vec{K}$	Present	Ref.33	Ref.77	Ref.13	Ref.11,12
(1,1,0)	16.29	16.27	16.32	15.88	15.78±.20
(2,0,0)	13.39	13.31	13.46	13.14±.34	13.13±.17
(2,1,1)	11.66	11.60	11.56	11.23±.34	11.47±.15
(2,2,0)	10.39	10.33	10.27	9.97±.50	10.20±.14
(3,1,0)	9.40	---	9.36	8.94±.30	---
(2,2,2)	8.82	---	8.70	8.44±.16	---
(3,2,1)	8.27	---	8.20	7.75±.10	---
(4,0,0)	7.76	---	7.81	7.50±.24	---
(3,3,0)	7.54	7.51	---	7.05±.09	---
(4,1,1)	7.48	7.45	---		---
(4,2,0)	7.23	---	---	6.72±.15	---
(3,3,2)	7.06	---	---	6.59±.19	---
(4,2,2)	6.84	---	---	6.41±.12	---
(4,3,1)	6.66	---	---	6.28±.09	---
(5,1,0)	6.59	---	---		---
(5,2,1)	6.33	---	---	5.96±.11	---
Ratio					
(330)/(411)	1.008	1.008	---	---	1.013±.007
(442)/(600)	1.014	---	---	---	1.014±.007

TABLE VIII

X-Ray Form Factors of Vanadium

$\frac{a}{2\pi\vec{K}}$	Present	Ref.9
(1,1,0)	15.752	15.90±.18
(2,0,0)	13.113	13.22±.17
(2,1,1)	11.434	---
(2,2,0)	10.229	---
(3,1,0)	9.323	---
(2,2,2)	8.727	---
(3,2,1)	8.216	---
(4,0,0)	7.778	---
(3,3,0)	7.516	---
(4,1,1)	7.487	---
(4,2,0)	7.239	---
(3,3,2)	7.046	---
(4,2,2)	6.842	---
(4,3,1)	6.671	---
(5,1,0)	6.636	---

Ratio	Present	Ref.77	Ref.10
(330)/(411)	1.0039	1.0015	1.0124
(442)/(600)	1.0065	1.0030	1.0237

TABLE IX

Compton Profiles of Chromium

q	J(100)	J(110)	J(111)	Jav
0.0	2.103	2.277	2.574	2.304
0.1	2.104	2.268	2.538	2.290
0.2	2.052	2.207	2.360	2.202
0.3	2.003	2.139	2.134	2.099
0.4	1.968	2.033	1.916	1.984
0.5	1.899	1.880	1.755	1.853
0.6	1.799	1.724	1.623	1.720
0.7	1.701	1.591	1.510	1.602
0.8	1.547	1.472	1.427	1.482
0.9	1.417	1.357	1.340	1.370
1.0	1.286	1.232	1.258	1.254
1.2	0.997	0.984	0.904	0.967
1.4	0.745	0.713	0.645	0.705
1.6	0.611	0.555	0.630	0.590
1.8	0.425	0.449	0.482	0.450
2.0	0.359	0.372	0.374	0.369
2.5	0.276	0.263	0.248	0.263
3.0	0.143	0.159	0.188	0.162
3.5	0.111	0.104	0.096	0.104
4.0	0.066	0.068	0.063	0.066
4.5	0.044	0.046	0.044	0.045
5.0	0.031	0.030	0.031	0.030

TABLE X

Compton Profiles of Vanadium

q	J(100)	J(110)	J(111)	Jav
0.0	1.765	2.139	2.255	2.062
0.1	1.832	2.162	2.260	2.093
0.2	2.006	2.139	2.171	2.109
0.3	2.077	2.012	1.987	2.025
0.4	1.950	1.870	1.853	1.889
0.5	1.798	1.692	1.662	1.714
0.6	1.678	1.552	1.517	1.579
0.7	1.588	1.370	1.395	1.439
0.8	1.491	1.234	1.309	1.327
0.9	1.214	1.148	1.240	1.190
1.0	0.850	1.042	0.963	0.967
1.2	0.625	0.765	0.624	0.689
1.4	0.657	0.509	0.502	0.550
1.6	0.429	0.395	0.469	0.424
1.8	0.327	0.304	0.349	0.322
2.0	0.253	0.264	0.289	0.267
2.5	0.225	0.181	0.148	0.185
3.0	0.105	0.100	0.110	0.104
3.5	0.076	0.065	0.057	0.066
4.0	0.042	0.042	0.042	0.042
4.5	0.024	0.027	0.028	0.026
5.0	0.018	0.018	0.017	0.018

TABLE XI

Transition Thresholds of Vanadium

	$\Sigma_1(E_f)-\Sigma_3$	$G_4(E_f)-G_1$	N_2-N_1,
Alward, et al., Ref. 87	2.16eV	2.27eV	2.73eV
Boyer, et al., Ref. 35	2.40	1.90	2.20
Koelling, Ref. 88	1.70	1.84	2.70
Present	2.09	1.52	2.53
Experiment (Rosei, et al., Ref. 84)	1.07	1.60	2.80

TABLE XII

Optical Conductivity and Joint Density of States versus Energy for Chromium

Energy(eV)	Re(σ(E)) (10^{15}sec^{-1})	G(E) (electrons/Ryd-atom)
0.0408	0.015993	0.10456
0.0816	0.078063	1.73288
0.1225	0.195152	3.85846
0.1633	0.323950	5.34506
0.2041	0.379112	6.45719
0.2449	0.428279	7.52744
0.2857	0.472777	8.56090
0.3265	0.536287	9.73950
0.3674	0.631996	11.29149
0.4082	0.718390	12.48259
0.4490	0.827146	13.82456
0.4898	0.939615	15.46978
0.5306	1.085780	17.35219
0.5714	1.224199	19.21927
0.6123	1.399872	21.34123
0.6531	1.664975	24.01055
0.6939	1.893553	26.94514
0.7347	2.067312	30.78177
0.7755	2.222800	34.66592
0.8163	2.475002	39.06197
0.8572	2.686766	42.18095
0.8980	2.920278	45.56662
0.9388	3.246675	51.29196
0.9796	3.559054	58.59960
1.0204	4.020492	69.15322
1.0613	4.710372	85.07279
1.1021	5.485455	101.18330
1.1429	6.117906	115.95520
1.1837	6.646346	131.21800
1.2245	6.502675	139.26950
1.2653	6.213130	145.54280
1.3062	6.178779	155.27560
1.3470	5.714201	158.10040
1.3878	5.506006	160.30800
1.4286	5.911606	170.15880
1.4694	6.286166	181.32840
1.5102	6.616663	192.89670
1.5511	6.915765	204.57530
1.5919	7.228439	216.51330
1.6327	7.535688	230.24910
1.6735	7.829554	244.86810
1.7143	8.158415	261.97120

Table XII (cont'd)

Energy(eV)	Re(σ(E))(10^{15}sec^{-1})	G(E) (electrons/Ryd-atom)
1.7551	8.676611	287.66350
1.7960	9.523974	324.71430
1.8368	10.066980	354.39080
1.8776	10.530910	380.92740
1.9184	10.081880	368.50960
1.9592	9.814885	366.57540
2.0001	9.102440	335.40690
2.0409	8.810443	325.29750
2.0817	8.731325	324.93190
2.1225	8.650773	323.94480
2.1633	8.714742	330.11530
2.2041	8.930560	345.09900
2.2450	9.166689	358.16110
2.2858	9.377490	373.28120
2.3266	9.597620	389.05530
2.3674	9.875917	397.81230
2.4082	10.251300	409.47320
2.4490	10.583680	422.40580
2.4899	10.797660	427.51150
2.5307	11.017500	434.08460
2.5715	11.389250	440.59240
2.6123	11.975850	451.91370
2.6531	12.358740	455.83460
2.6939	12.562740	458.07810
2.7348	12.590340	460.88510
2.7756	12.684760	465.45280
2.8164	12.795580	470.32820
2.8572	13.067460	478.77090
2.8980	13.402140	489.70150
2.9389	13.767770	498.16870
2.9797	14.280230	510.69040
3.0205	14.269160	508.93290
3.0613	14.888500	516.59050
3.1021	15.499060	525.78730
3.1429	15.966470	536.64270
3.1838	16.255180	545.68320
3.2246	14.181900	516.36240
3.2654	12.901290	494.76710
3.3062	12.020240	483.46380
3.3470	11.168650	474.80050
3.3878	10.389800	465.08190
3.4287	10.298860	473.70450
3.4695	10.688250	479.91770
3.5103	10.228400	465.98720
3.5511	9.029546	445.24120
3.5919	8.648007	444.63210

Table XII (cont'd)

Energy(eV)	Re(σ(E))(10^{15}sec^{-1})	G(E) (electrons/Ryd-atom)
3.6327	8.478111	450.04530
3.6736	8.304706	464.12240
3.7144	8.335518	483.10710
3.7552	8.619647	524.30700
3.7960	8.989955	558.61110
3.8368	9.836828	644.12760
3.8777	10.256170	699.93970
3.9185	10.109160	666.07510
3.9593	8.964924	486.85240
4.0001	8.992949	464.25870
4.0409	7.571873	413.85830
4.0817	7.115709	400.94840
4.1226	6.910714	399.18180
4.1634	6.872777	413.13230
4.2042	7.361943	460.09610
4.2450	6.455207	408.17730
4.2858	5.989615	390.32270
4.3266	5.668940	379.11160
4.3675	5.386898	368.33230
4.4083	5.128178	361.64300
4.4491	4.838272	353.38570
4.4899	4.543697	340.43360
4.5307	4.297181	329.96320
4.5715	4.108143	325.34420
4.6124	3.943228	322.90890
4.6532	3.782704	321.65540
4.6940	3.633950	319.72470
4.7348	3.505387	318.23010
4.7756	3.405882	317.53030
4.8165	3.341114	320.73920
4.8573	3.287752	324.98500
4.8981	3.242098	328.67960
4.9389	3.205520	333.29310
4.9797	3.224041	339.23030
5.0205	3.357245	349.81170
5.0614	3.362365	356.26490
5.1022	3.293901	359.59830
5.1430	3.197293	359.41630
5.1838	3.092646	358.54500
5.2246	2.938237	355.01610
5.2654	2.828121	353.23910
5.3063	2.740030	349.78920
5.3471	2.645340	345.57170
5.3879	2.540051	336.28890
5.4287	2.429133	306.38540
5.4695	2.373932	299.81410

Table XII (cont'd)

Energy (eV)	Re(σ(E)) (10^{15} sec^{-1})	G(E) (electrons/Ryd-atom)
5.5103	2.349702	299.36640
5.5512	2.313246	298.08990
5.5920	2.254443	297.11560
5.6328	2.211760	296.25470
5.6736	2.189775	297.42490
5.7144	2.213548	303.74890
5.7553	2.221272	300.35500
5.7961	2.172669	291.75100
5.8369	2.132226	285.46140
5.8777	2.099352	281.44710
5.9185	2.023370	277.72650
5.9593	1.884438	270.05780
6.0002	1.758421	259.96560
6.0410	1.647548	240.26970
6.0818	1.597747	228.48900
6.1226	1.655611	222.32220
6.1634	1.857006	221.78170
6.2042	2.300002	234.43110
6.2451	3.308958	259.73960
6.2859	5.354712	293.58470
6.3267	8.572866	339.90720
6.3675	8.101730	327.20260
6.4083	6.848334	302.69760
6.4491	6.297358	292.82660
6.4900	6.190581	283.22570
6.5308	5.460226	257.09380
6.5716	4.902838	233.20660
6.6124	4.345373	205.85990
6.6532	3.984561	189.93450
6.6941	3.730206	181.97430
6.7349	3.562893	176.69610
6.7757	3.410551	171.42440
6.8165	3.248170	165.48430

TABLE XIII

Optical Conductivity and Joint Density of States versus Energy for Vanadium

Energy (eV)	Re(σ(E)) (10^{15} sec^{-1})	G(E) (electrons/Ryd-atom)
0.0408	0.303250	3.87029
0.0816	0.592211	19.58297
0.1225	0.951341	38.14514
0.1633	0.462290	34.15234
0.2041	0.334549	42.13629
0.2449	0.233620	36.12670
0.2857	0.186686	20.60281
0.3265	0.185148	10.37869
0.3674	0.214237	7.96885
0.4082	0.245445	9.05168
0.4490	0.264424	9.96637
0.4898	0.281406	10.74998
0.5306	0.299511	11.31034
0.5714	0.316565	11.56559
0.6123	0.331212	12.39579
0.6531	0.406421	17.72066
0.6939	0.513727	24.00532
0.7347	0.603495	28.33560
0.7755	0.694103	32.37491
0.8163	0.781100	35.80323
0.8572	0.863809	39.12071
0.8980	0.942600	42.70738
0.9388	1.003178	46.16207
0.9796	1.043590	49.45022
1.0204	1.070020	52.63346
1.0613	1.087071	55.39388
1.1021	1.098555	57.96374
1.1429	1.104907	60.63795
1.1837	1.105424	63.47725
1.2245	1.102101	67.24843
1.2653	1.094126	68.30151
1.3062	1.091794	68.60408
1.3470	1.125282	69.98388
1.3878	1.333103	75.69068
1.4286	1.545656	80.85308
1.4694	1.731544	85.94002
1.5102	1.928939	91.73490
1.5511	2.165241	98.30935
1.5919	2.607301	107.70290
1.6463	3.015267	118.44490
1.6871	3.255473	125.82940
1.7279	3.529076	134.66340

Table XIII (cont'd)

Energy(eV)	Re(σ(E)) (10^{15}sec^{-1})	G(E) (electrons/Pyd-atom)
1.7688	3.915360	146.41940
1.8096	4.173240	156.65260
1.8504	4.527862	172.00750
1.8912	4.899136	190.34830
1.9320	5.144379	206.77710
1.9728	5.580387	236.95920
2.0137	5.954113	271.10590
2.0545	6.077293	280.22670
2.0953	5.683711	264.09970
2.1361	5.407372	256.73640
2.1769	5.318402	257.06050
2.2177	5.297108	263.92360
2.2586	5.315804	275.42340
2.2994	5.361846	289.13480
2.3402	5.416684	302.51020
2.3810	5.468219	311.17780
2.4218	5.539614	322.21570
2.4626	5.690419	336.20690
2.5035	5.898214	351.64880
2.5443	6.464527	369.88350
2.5851	6.729630	380.68570
2.6259	6.986928	387.38340
2.6667	7.441928	398.44190
2.7076	8.388711	415.91620
2.7484	9.083706	429.77440
2.7892	9.513228	442.24740
2.8300	10.001010	457.44320
2.8708	10.491070	470.17770
2.9116	10.927860	481.16190
2.9525	11.351100	491.72400
2.9933	11.980680	506.94860
3.0341	12.628500	520.38130
3.0749	13.082530	530.84300
3.1157	13.606960	542.80240
3.1565	14.097010	552.25900
3.1974	14.534240	564.84430
3.2382	14.633100	567.04860
3.2790	14.721560	574.07650
3.3198	14.421400	569.12060
3.3606	13.834180	564.73610
3.4014	12.535400	532.60890
3.4423	12.107340	523.83740
3.4831	11.370050	509.44620
3.5239	10.343120	487.43430
3.5647	10.211670	493.40140
3.6055	9.266482	491.40420

Table XIII (cont'd)

Energy(eV)	Pe(σ(E))(10^{15}sec^{-1})	G(E)(electrons/Ryd-atom)
3.6464	8.915588	495.48410
3.6872	8.780803	498.28320
3.7280	9.241172	525.31200
3.7688	9.350045	554.45580
3.8096	9.511574	633.16800
3.8504	9.732486	729.06690
3.8913	10.677840	891.39430
3.9321	9.446235	596.26110
3.9729	8.136292	452.77780
4.0137	7.001424	406.73870
4.0545	6.511905	386.28020
4.0953	6.247554	376.20630
4.1362	6.132642	378.37000
4.1770	6.072959	385.51550
4.2178	6.454335	435.47510
4.2586	5.578785	385.97770
4.2994	5.239748	378.39000
4.3403	4.866563	364.45000
4.3811	4.566426	353.86580
4.4219	4.311811	345.28990
4.4627	4.072380	336.15630
4.5035	3.879421	331.55800
4.5443	3.724182	328.76830
4.5852	3.576118	327.12780
4.6260	3.436652	324.29850
4.6668	3.315216	322.65470
4.7076	3.205593	321.73150
4.7484	3.109102	323.15090
4.7892	3.027366	326.85940
4.8301	2.964340	332.27170
4.8709	2.899205	335.58650
4.9117	2.847297	340.56060
4.9525	2.818271	347.06170
4.9933	2.805005	355.08220
5.0341	2.894679	364.17370
5.0750	3.004566	373.12940
5.1158	3.048755	379.85010
5.1566	2.959123	378.09670
5.1974	2.867713	376.93310
5.2382	2.781096	377.49020
5.2790	2.688779	378.53850
5.3199	2.553644	372.89970
5.3607	2.451233	368.35230
5.4015	2.382883	342.68460
5.4423	2.336820	334.25070
5.4831	2.278223	329.53320

Table XIII (cont'd)

Energy(eV)	Re(σ(E))(10^{15}sec^{-1})	G(E) (electrons/Ryd-atom)
5.5240	2.198058	325.42630
5.5648	2.136530	323.69990
5.6056	2.100289	325.28090
5.6464	2.080417	324.87940
5.6872	2.052576	323.93960
5.7280	2.034515	329.94550
5.7689	2.025528	322.91590
5.8097	2.011952	316.91890
5.8505	1.980614	311.23990
5.8913	1.960362	303.99410
5.9321	1.896332	291.96180
5.9729	1.830106	276.43820
6.0138	1.706723	262.27930
6.0546	1.553814	244.38940
6.0954	1.474626	234.80370
6.1362	1.501627	229.56750
6.1770	1.673391	225.81430
6.2178	2.064022	233.30210
6.2587	3.962298	274.57100
6.2995	8.529045	370.15910
6.3403	7.521153	354.33300
6.3811	6.335064	332.65010
6.4219	5.728550	313.67580
6.4628	5.518938	306.51560
6.5036	5.222835	299.53970
6.5444	5.096507	295.25980
6.5852	4.853708	279.64900
6.6260	4.639256	274.73000
6.6668	4.097979	249.18560
6.7077	3.699172	224.22540
6.7485	3.485639	212.93060
6.7893	3.300007	194.18310

FIGURE CAPTIONS

Figure		Page
I	Band structure of chromium obtained with the KSG exchange-correlation potential along the symmetry axes. The horizontal line indicates the Fermi energy. Each band is labelled according to its symmetry...	86
II	Band structure of chromium obtained with the VBH exchange-correlation potential along the symmetry axes.....	87
III	Comparison of our KSG bands with the results of the angle-resolved photo-emission experiment of Johansson, et al. (Ref. 60). In order to approximate the antiferromagnetic structure, our (para-magnetic bands along $\overline{NH}$ (dashed lines) have been folded back over those along $\overline{\Gamma N}$ (solid lines). The circles and crosses represent experimental results at different incident photon directions (15° and 75°, respectively, from the normal to the surface).....	88
IV	Band structure of vanadium obtained with the KSG potential along the symmetry axes.....	89
V	Density of states for the band electrons (3d, 4s) and the next higher-energy states (4p) of chromium (KSG potential).....	90
VI	Density of states for the band electrons (solid line) and the integrated number of electrons (dashed line) of chromium (VBH potential).....	91
VII	Density of states for the band electrons of vanadium (KSG potential).....	92
VIII	Fermi surface of chromium. Although the results of the VBH potential are the only ones shown, the results from the two potentials are practically in-distinguishable. The first Brillouin zone has been outlined. (a) The band 3 hole pockets at H and hole ellipsoids	

Figure Captions (cont'd)

Figure		Page
	at N (the center of each face of the Brillouin zone). (b) The band 4 electron "jack" centered at Γ (the center of the Brillouin zone). (c) The band 5 electron "lenses" are the result of the overlap of the body of the jack with the balls.....	93
IX	Fermi surface cross-sections of chromium (VBH potential). All bands have been included and the results of the neighboring Brillouin zones have been added. (a) The (001) plane that passes through Γ (i.e., the plane with k_z=0). (b) The (011) plane that passes through Γ.....	96
X	Fermi surface of vanadium. (a) The band 2 hole surface surrounding Γ. (b) The band 3 hole ellipsoids at the N points and the open "jungle-gym" structure which extends from Γ to H.....	98
XI	Fermi surface cross-section of vanadium. The (001) plane that passes through Γ.....	100
XII	Spherically-averaged Compton profile of chromium. The experimental results of Paakkari, et al. (Ref. 23) are represented by circles and some typical error bars have been included.....	101
XIII	Anisotropy of the Compton profile of chromium as indicated by the difference between the profiles in the [111] and [100] directions. The data of Weiss (Ref. 24) is represented by squares.....	102
XIV	Spherically-averaged Compton profile of vanadium. The data points (circles) and error bars represent the results of Phillips (Ref. 25).....	103

Figure Captions (cont'd)

Figure		Page
XV	Anisotropy of the Compton profile of vanadium	104
XVI	Optical conductivity of chromium. Curve A is the calculated interband conductivity. The result in curve B has been smoothed (0.5 eV smoothing) and includes the Drude intraband term. The self-energy correction with λ=-0.1 has been used to generate curve C. The results of Nestell and Christy (Ref. 20) are represented by squares and those of Ganin, et al. (Ref. 18) by circles	105
XVII	Optical conductivity of vanadium. The labelling of curves A, B and C corresponds to that used in Figure XVI. The experimental results of Nestell and Christy (Ref. 20) are also displayed	106
XVIII	Electron energy-loss spectrum of chromium. The solid (——) line is the result of our interband calculation in the sharp limit and the dash-dot line (-.-.-) is our smoothed result including the Drude contribution. The dashed line (---) was derived from the data of Nestell and Christy (Ref. 20) and the dotted line (····) was obtained from Lynch (Ref. 89)	107

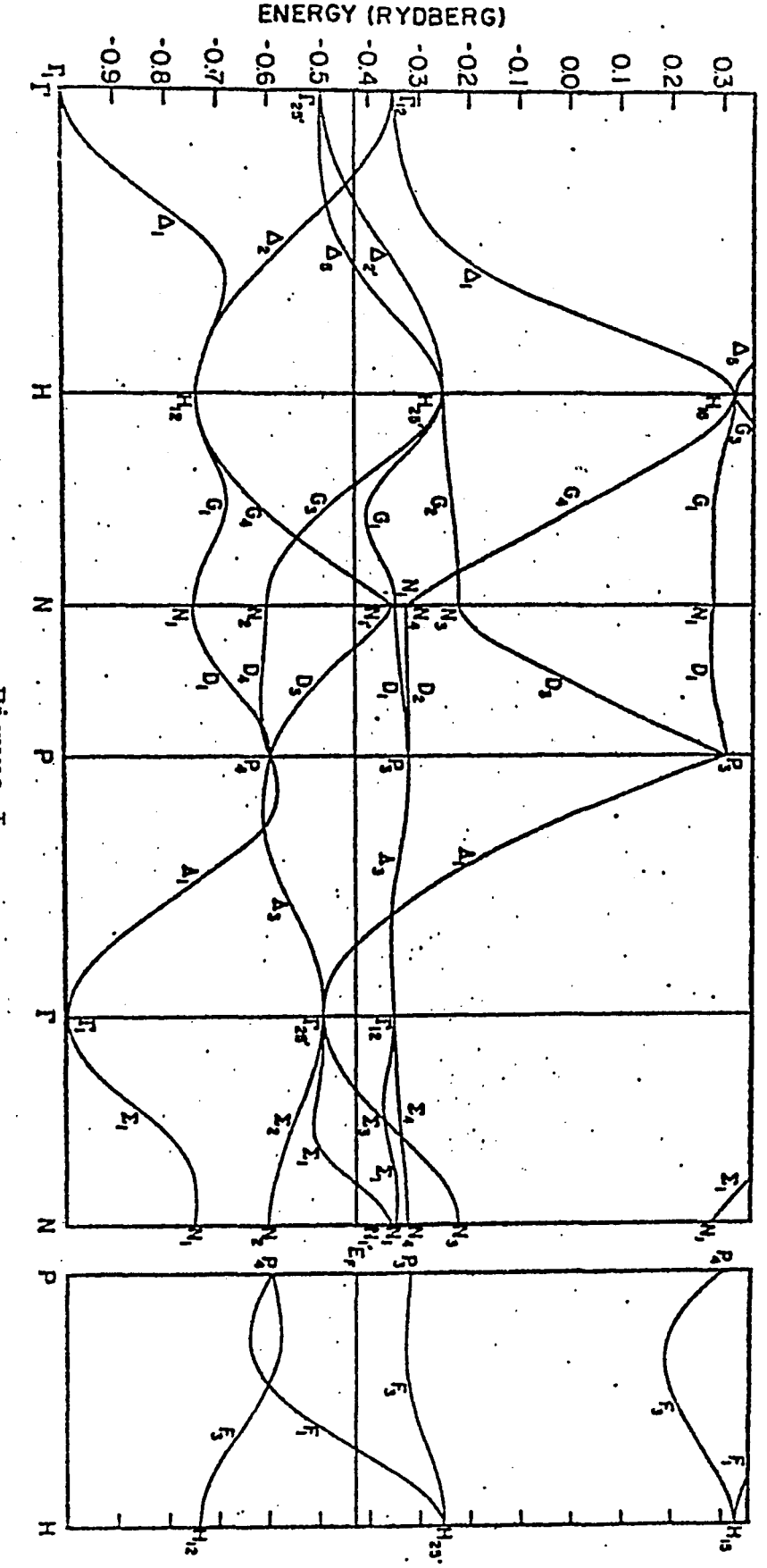

Figure I

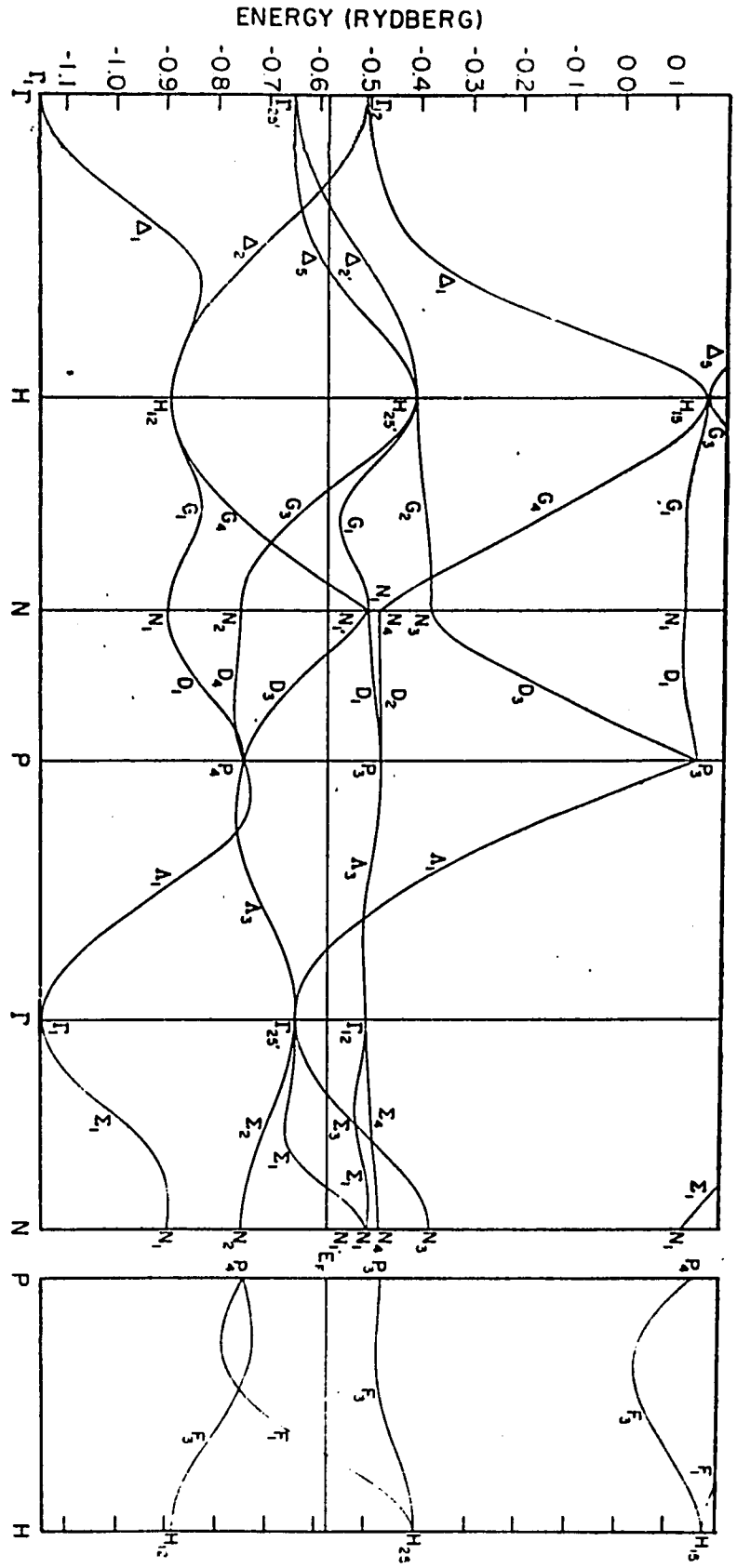

Figure II

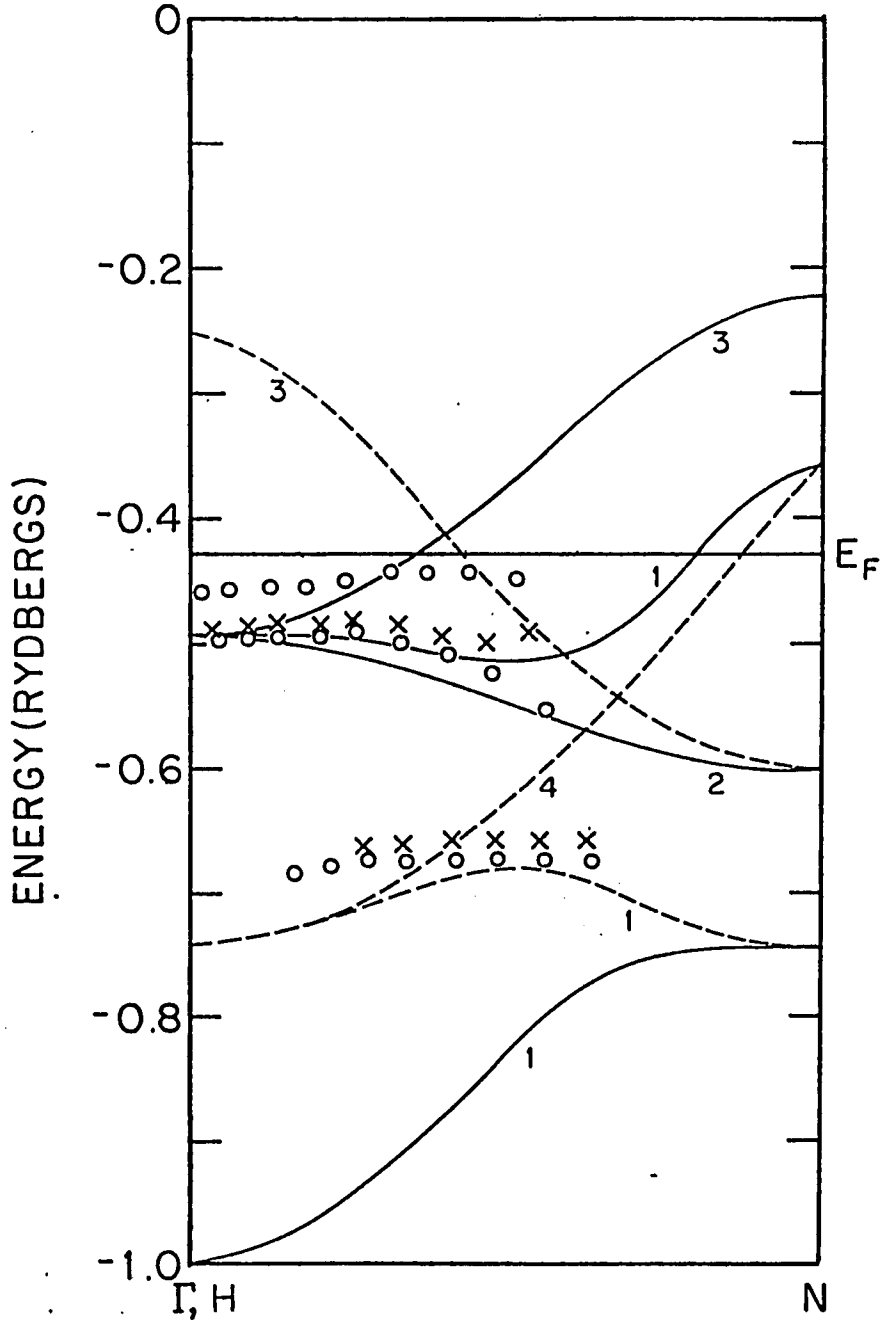

Figure III

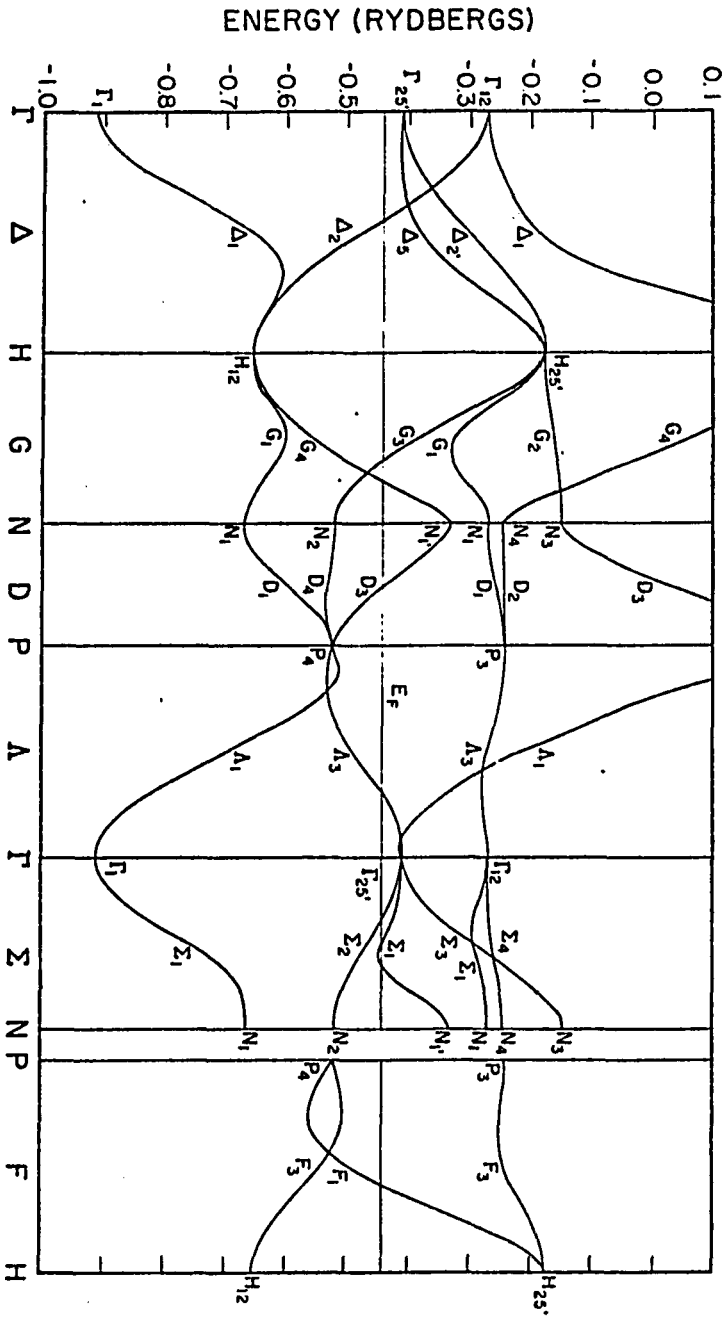
ENERGY (RYDBERGS)
0.1
0.0
-0.1
-0.2
-0.3
-0.5
-0.6
-0.7
-0.8
-1.0
Γ
Δ
H
G
N
D
P
Λ
Γ
Σ
N
P
F
H
E_F

Figure IV

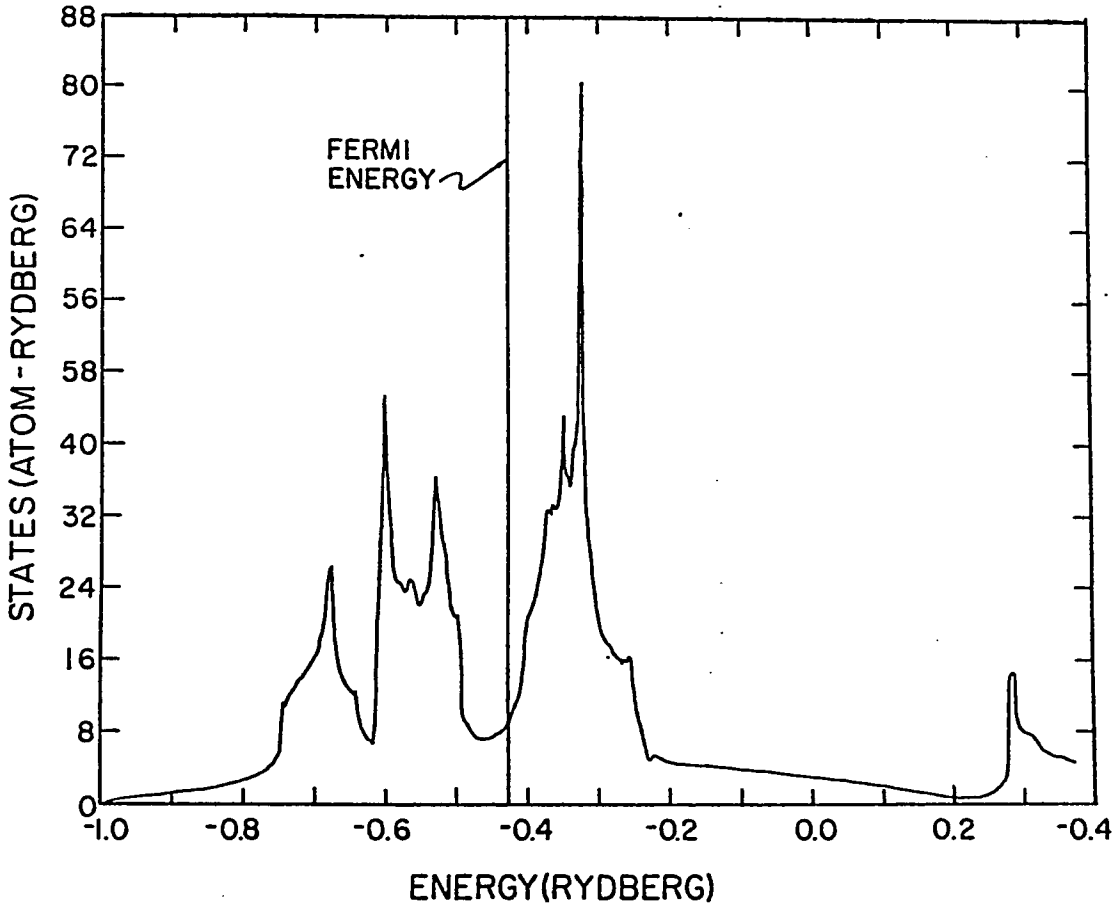
88
80
72
64
56
58
40
32
24
16
8
0
FERMI
ENERGY
STATES (ATOM-RYDBERG)
-1.0
-0.8
-0.6
-0.4
-0.2
0.0
0.2
-0.4
ENERGY (RYDBERG)

Figure V

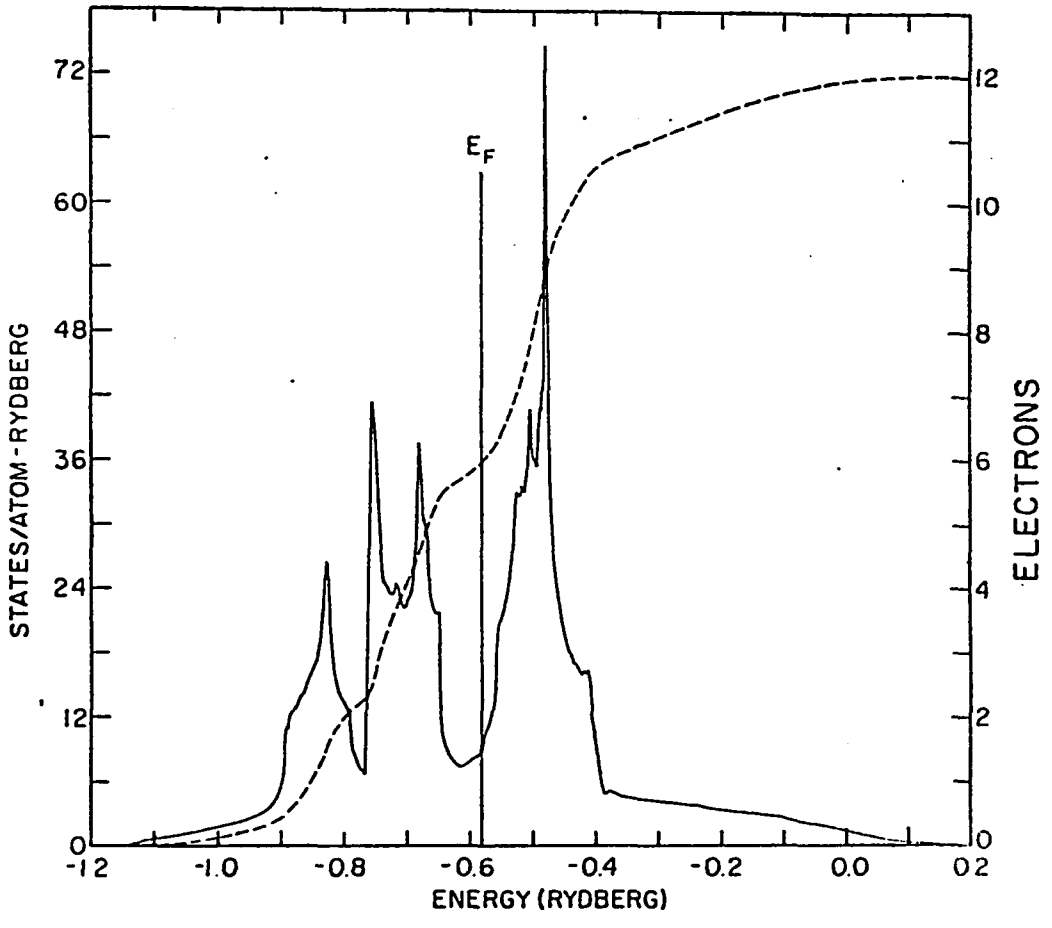
72
60
48
36
24
12
0
STATES/ATOM-RYDBERG
E_F
12
10
8
6
4
2
0
ELECTRONS
-1.2
-1.0
-0.8
-0.6
-0.4
-0.2
0.0
0.2
ENERGY (RYDBERG)

Figure VI

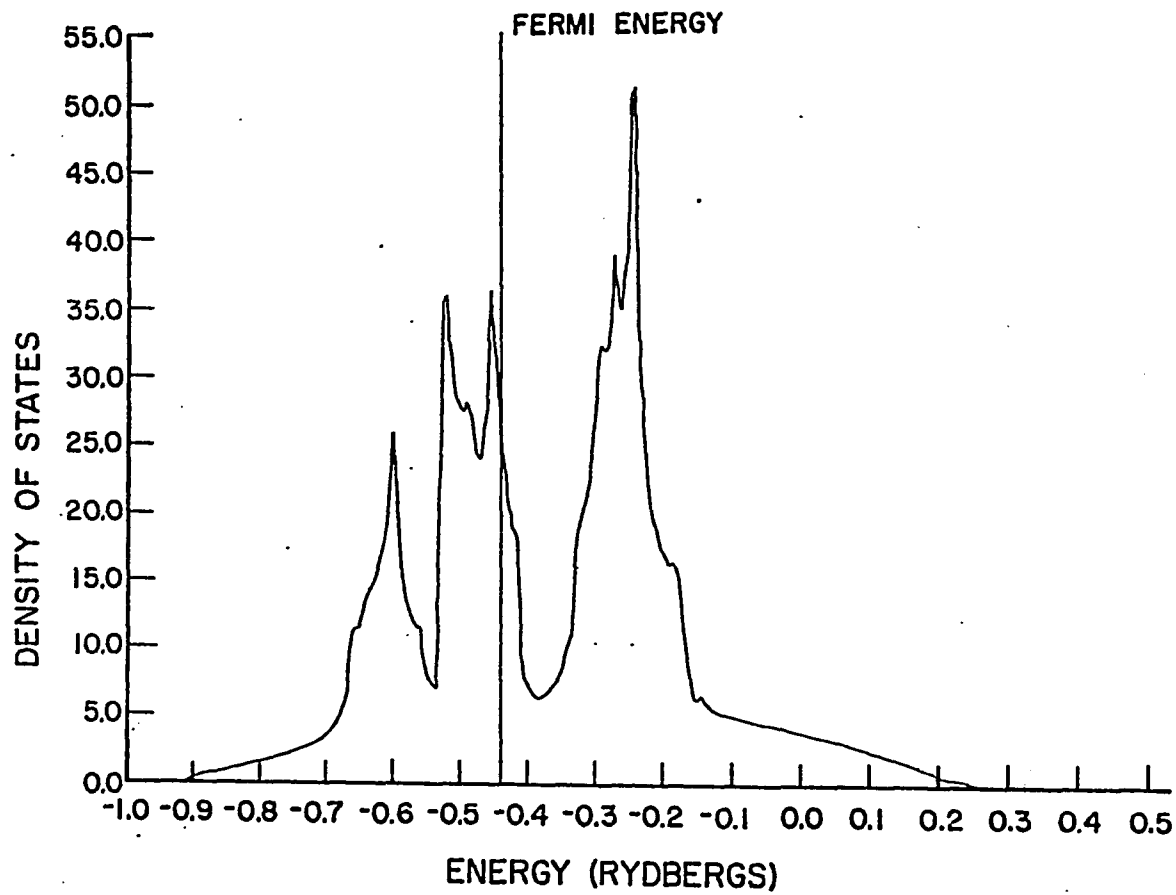
FERMI ENERGY
55.0
50.0
45.0
40.0
35.0
30.0
25.0
20.0
15.0
10.0
5.0
0.0
DENSITY OF STATES
-1.0 -0.9 -0.8 -0.7 -0.6 -0.5 -0.4 -0.3 -0.2 -0.1 0.0 0.1 0.2 0.3 0.4 0.5
ENERGY (RYDBERGS)

Figure VII

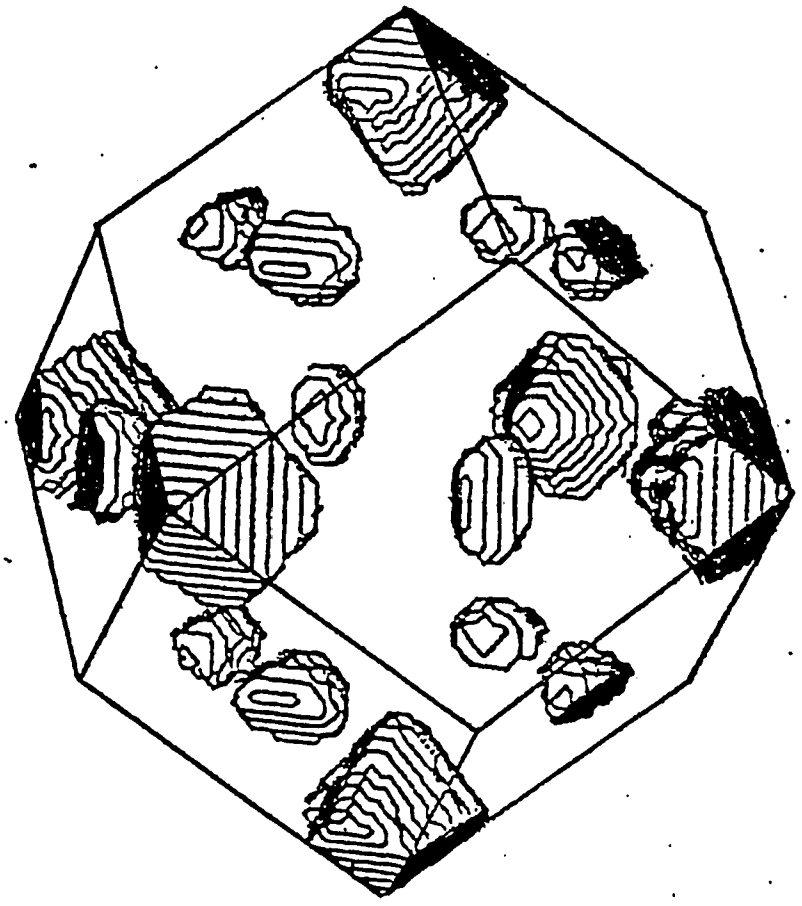

Figure VIII (a)

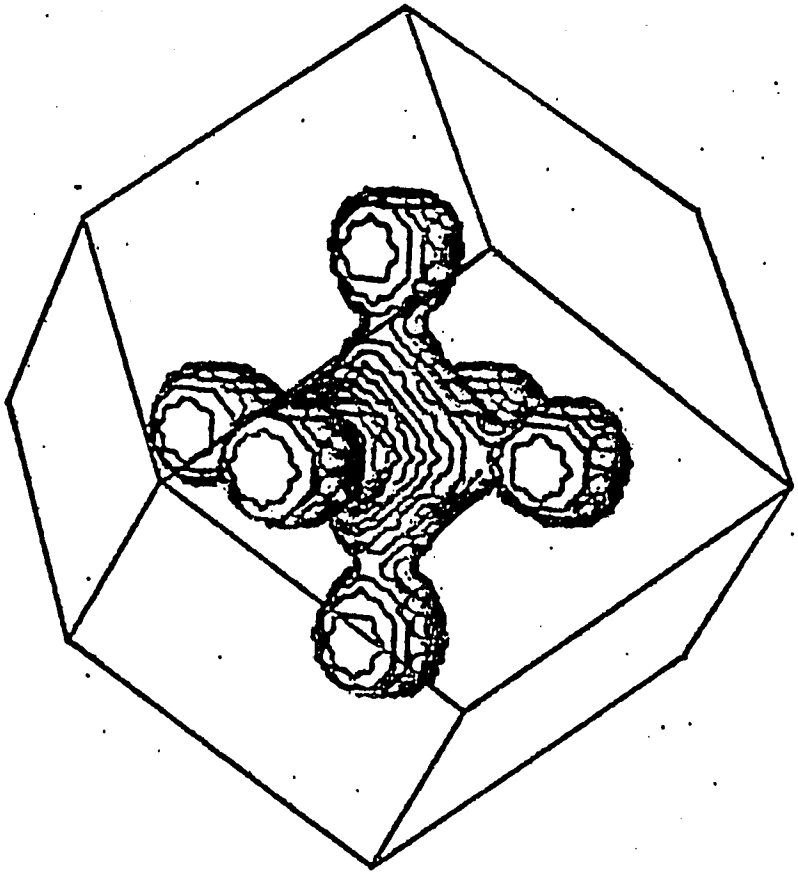

Figure VIII (b)

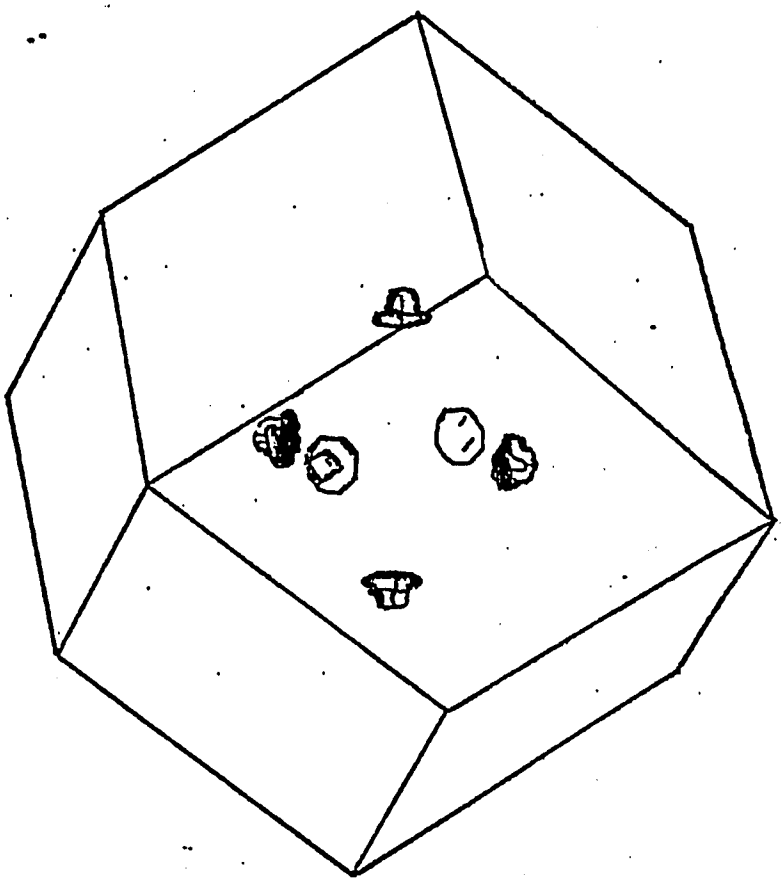

Figure VIII (c)

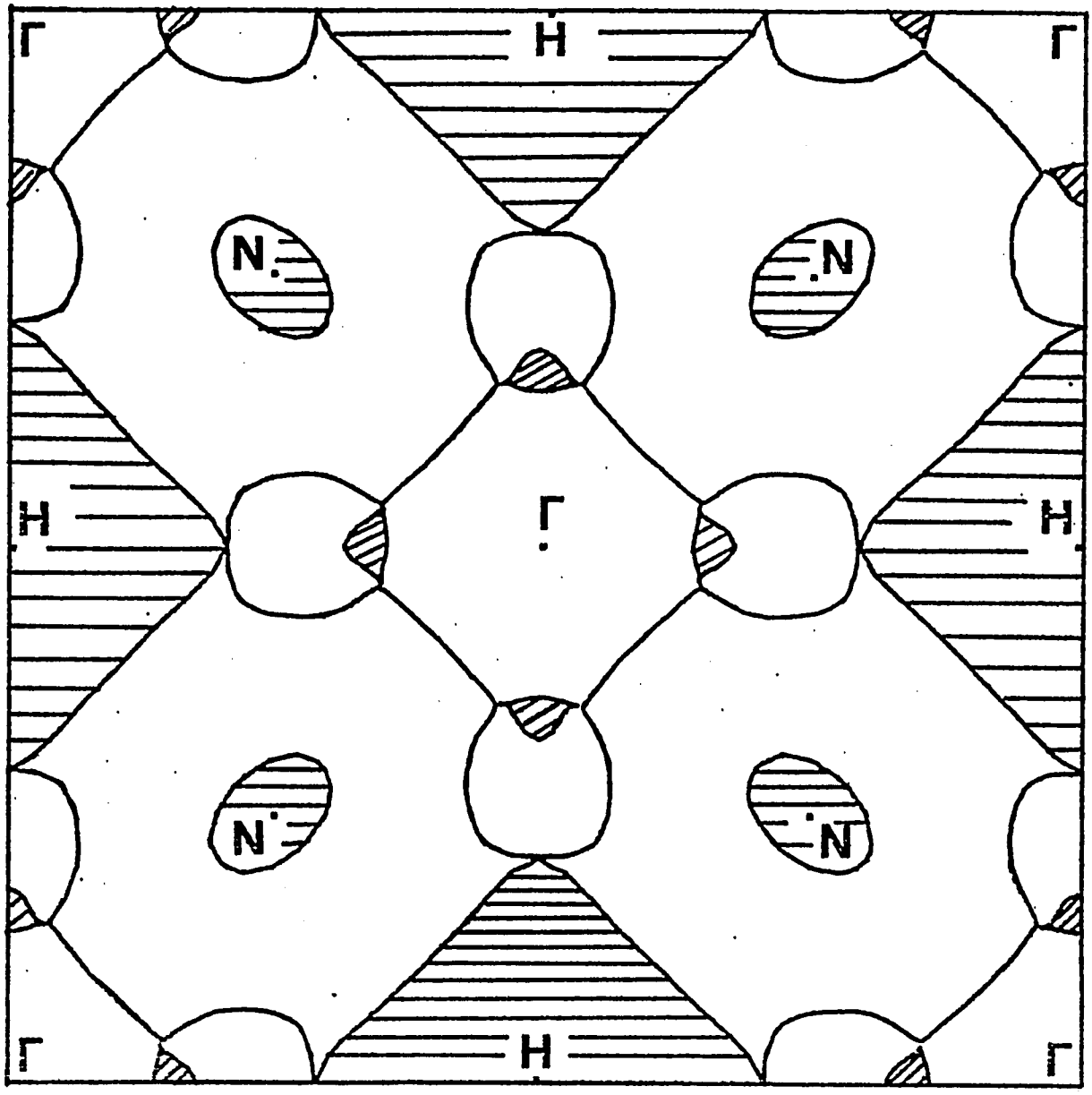

Figure IX. (a)

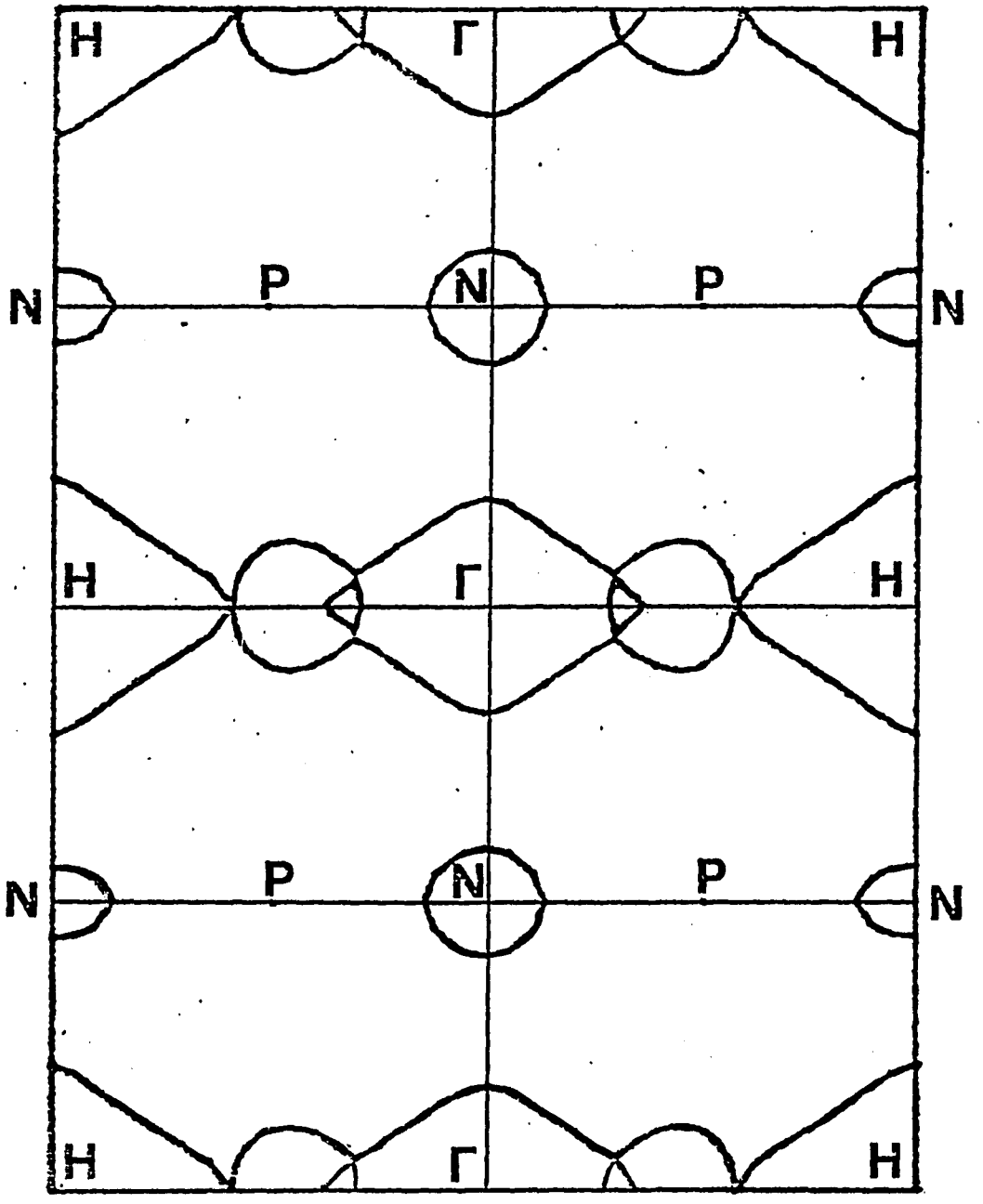

Figure IX (b)

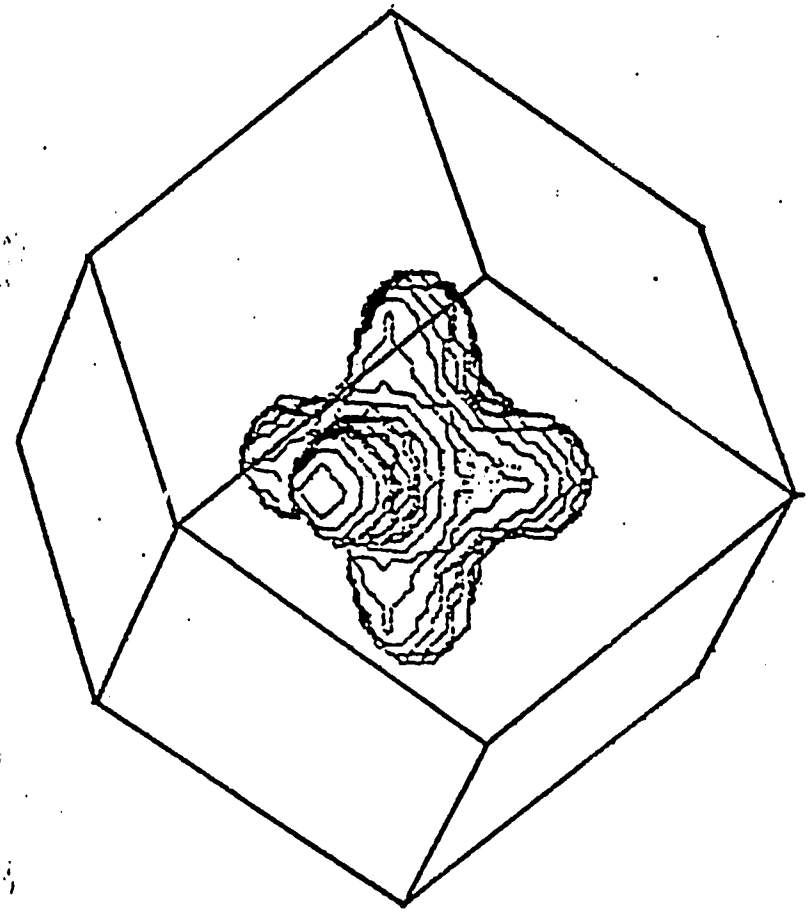

Figure X (a)

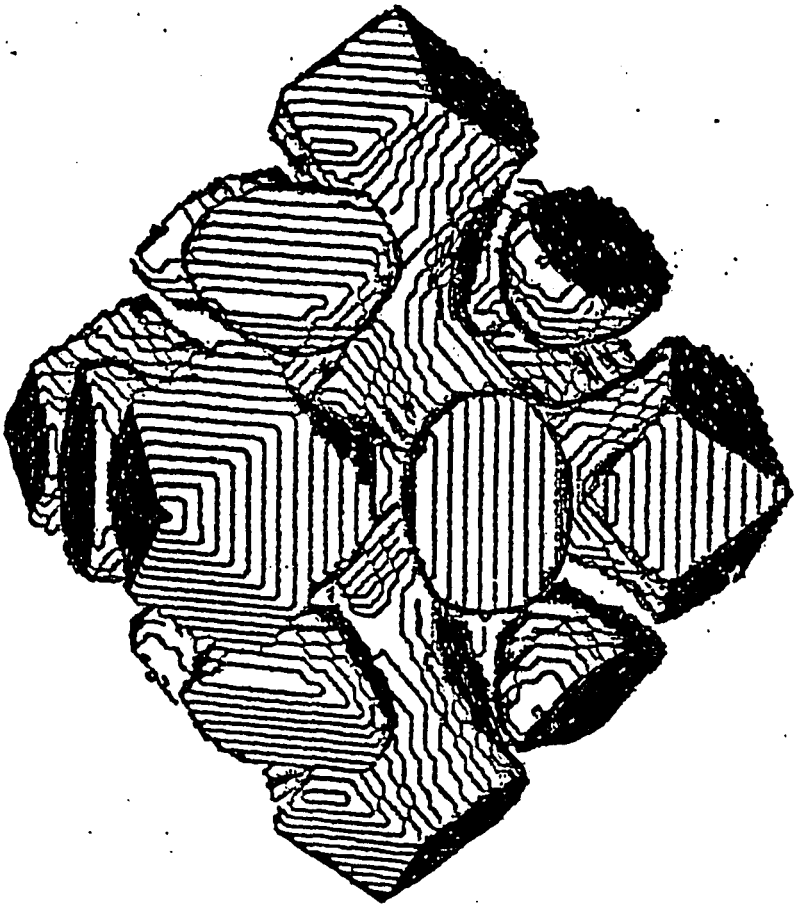

Figure X (b)

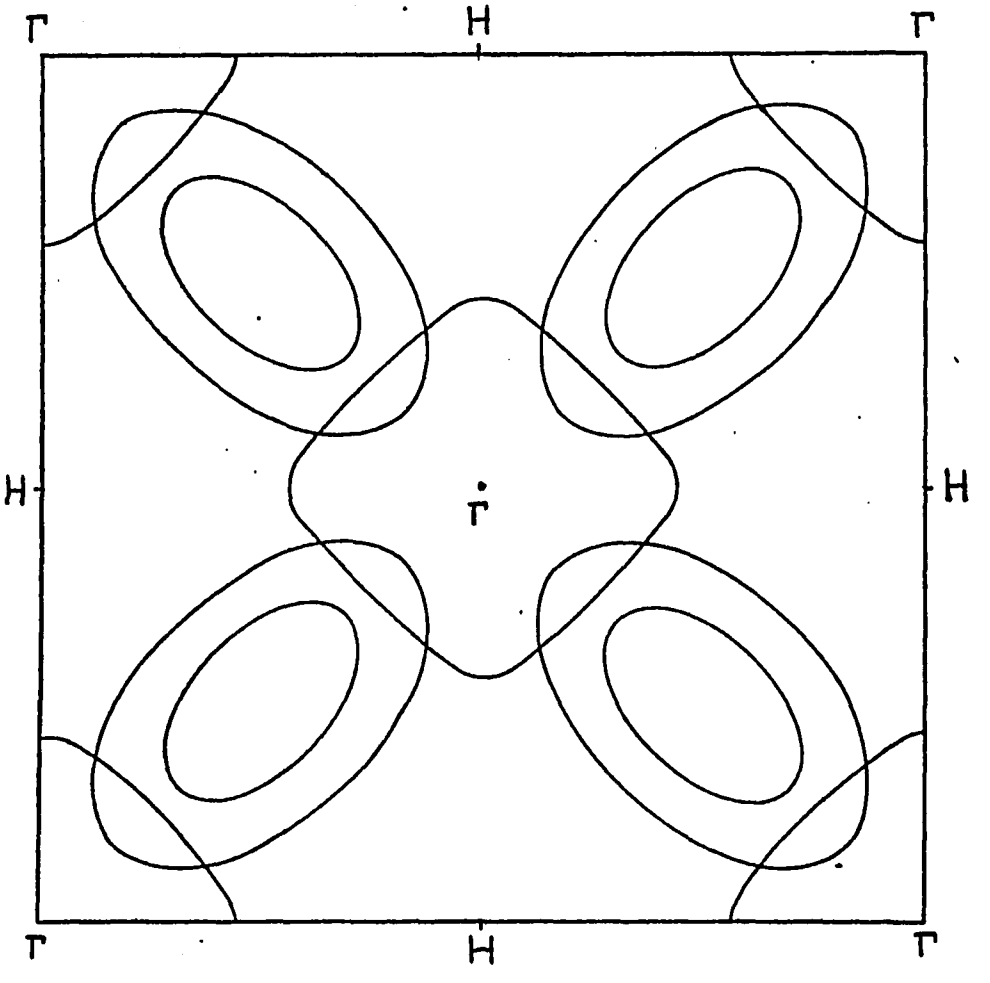

Figure XI

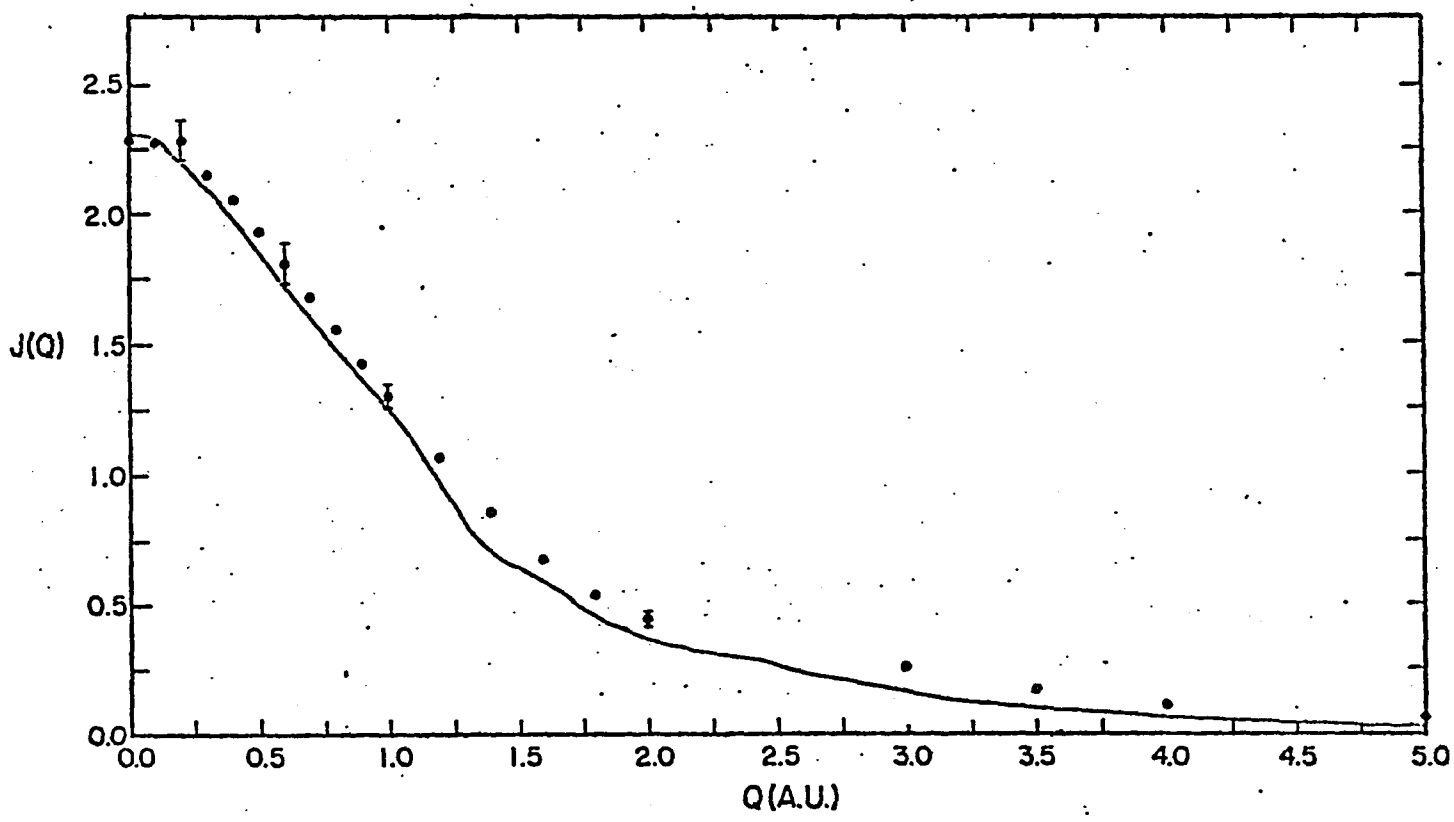

Figure XII

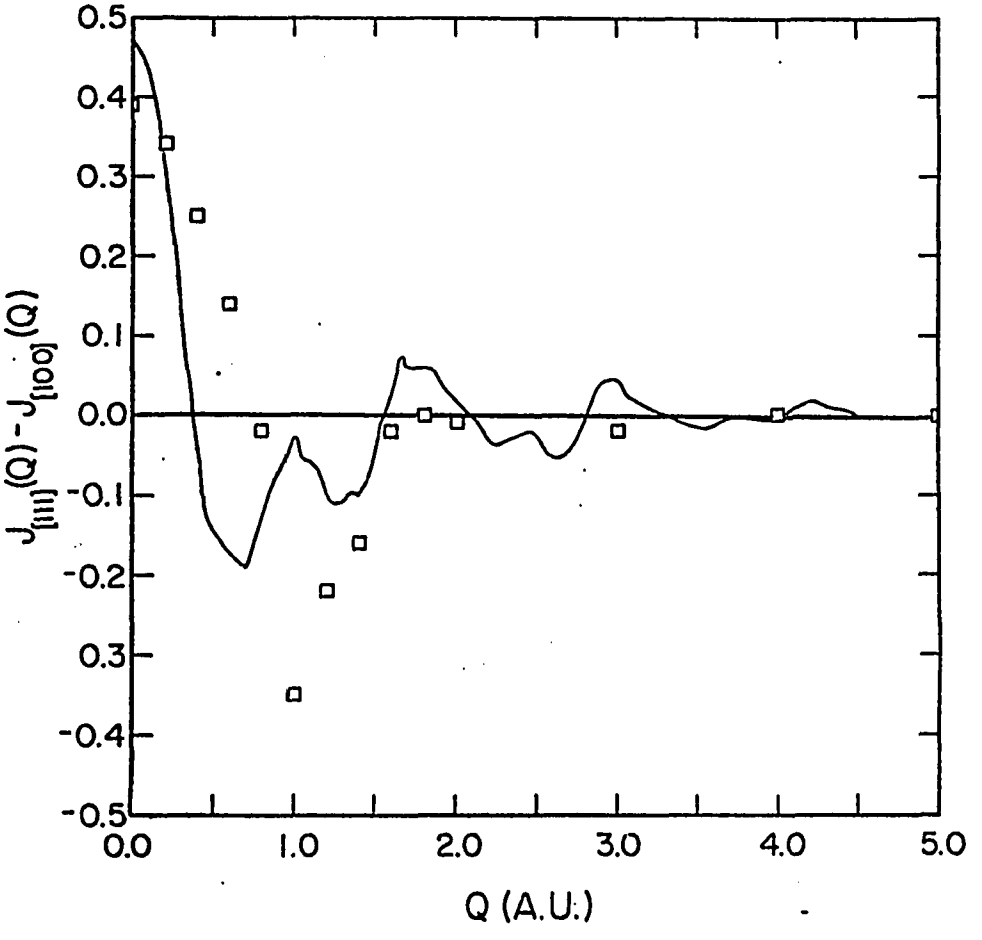

Figure XIII

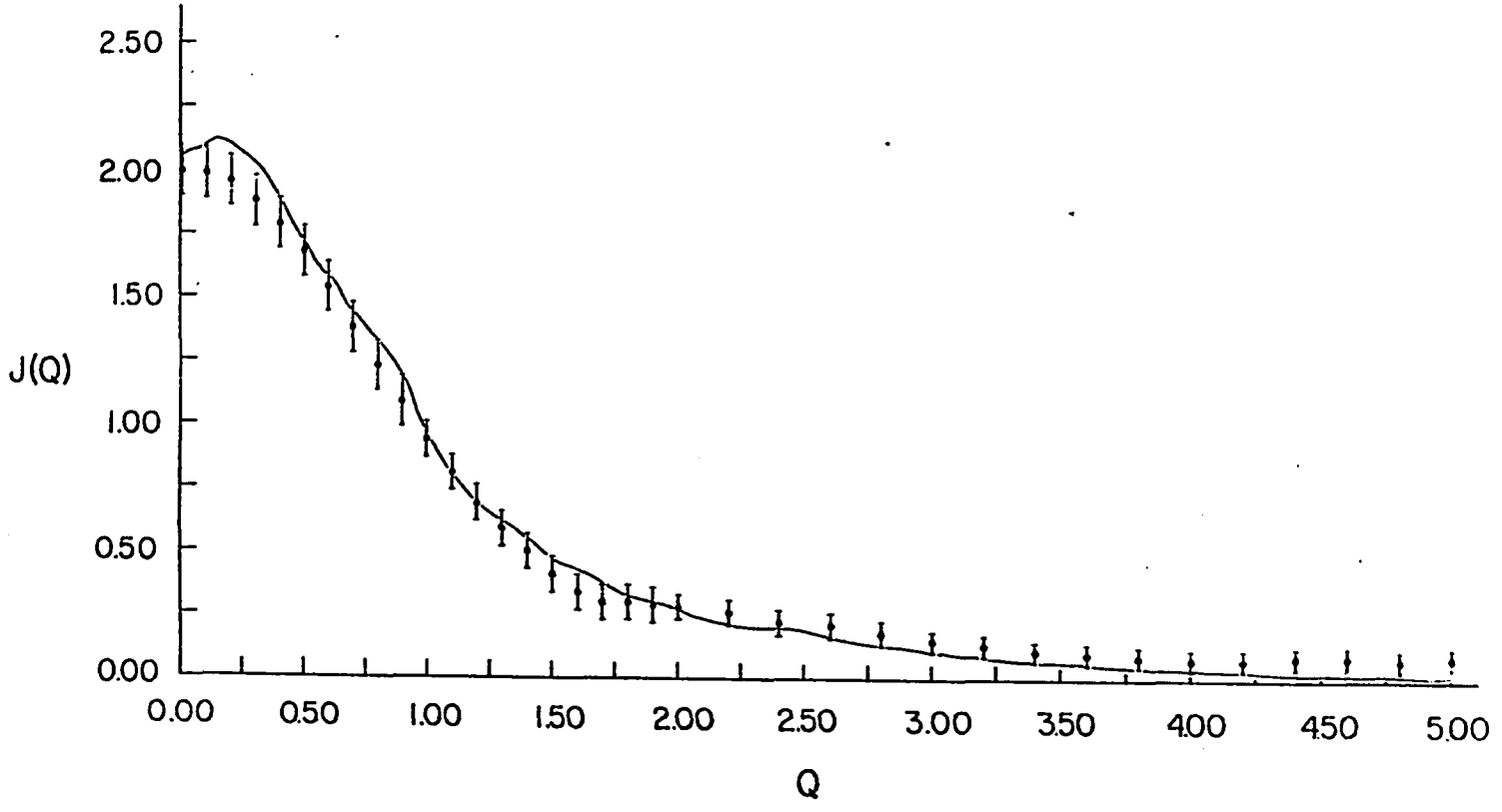
2.50
2.00
1.50
1.00
0.50
0.00
J(Q)
0.00
0.50
1.00
1.50
2.00
2.50
3.00
3.50
4.00
4.50
5.00
Q

Figure XIV

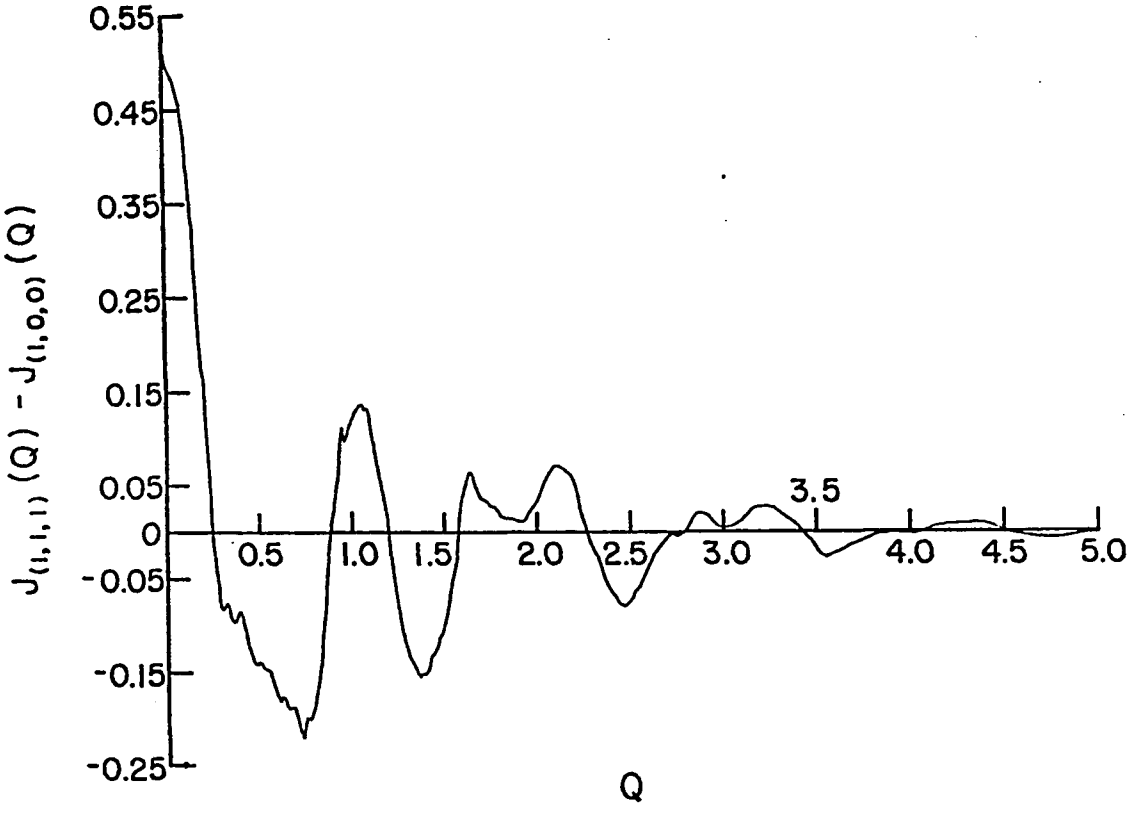
0.55
0.45
0.35
0.25
0.15
0.05
0
-0.05
-0.15
-0.25
0.5
1.0
1.5
2.0
2.5
3.0
3.5
4.0
4.5
5.0
Q
J(1,1,1) (Q) - J(1,0,0) (Q)

Figure XV

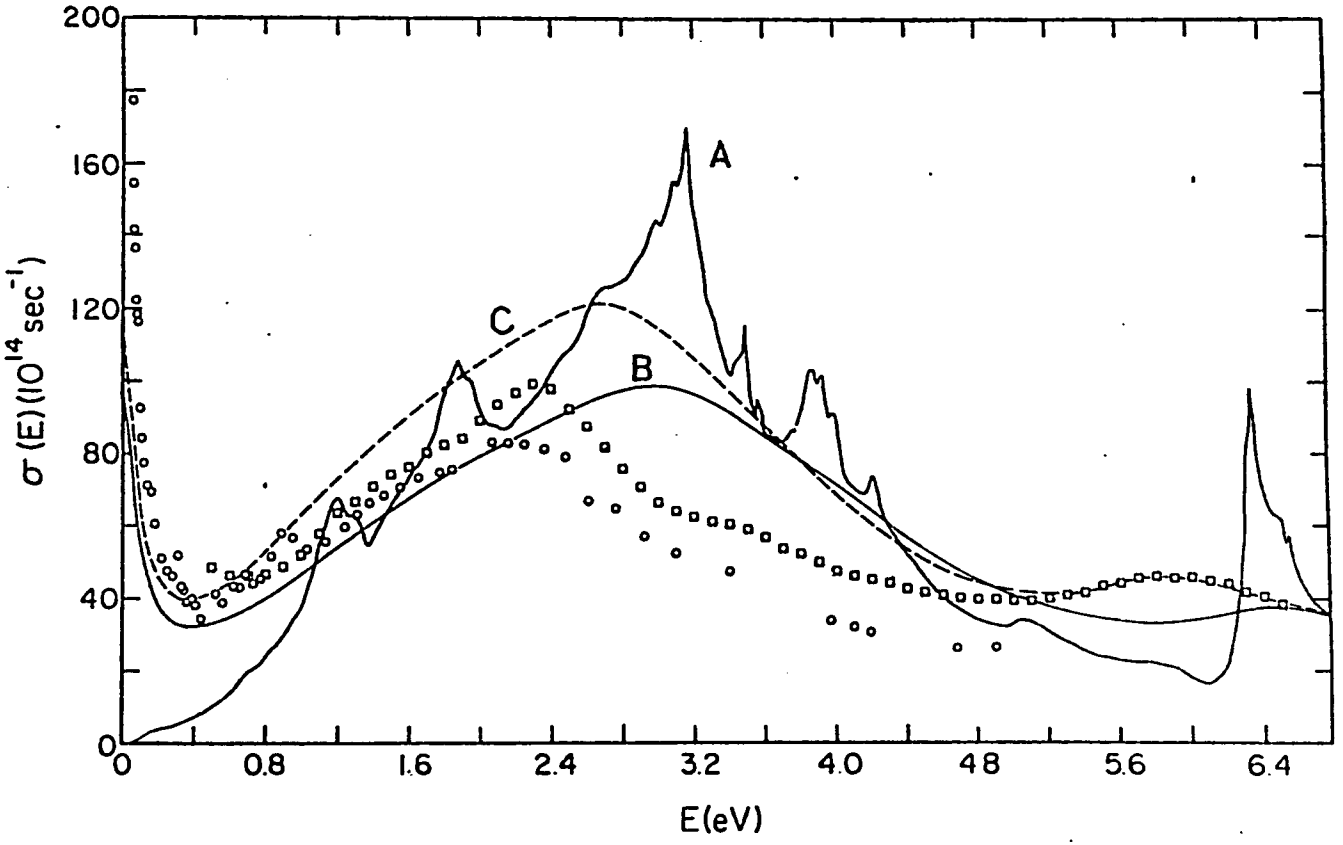

Figure XVI

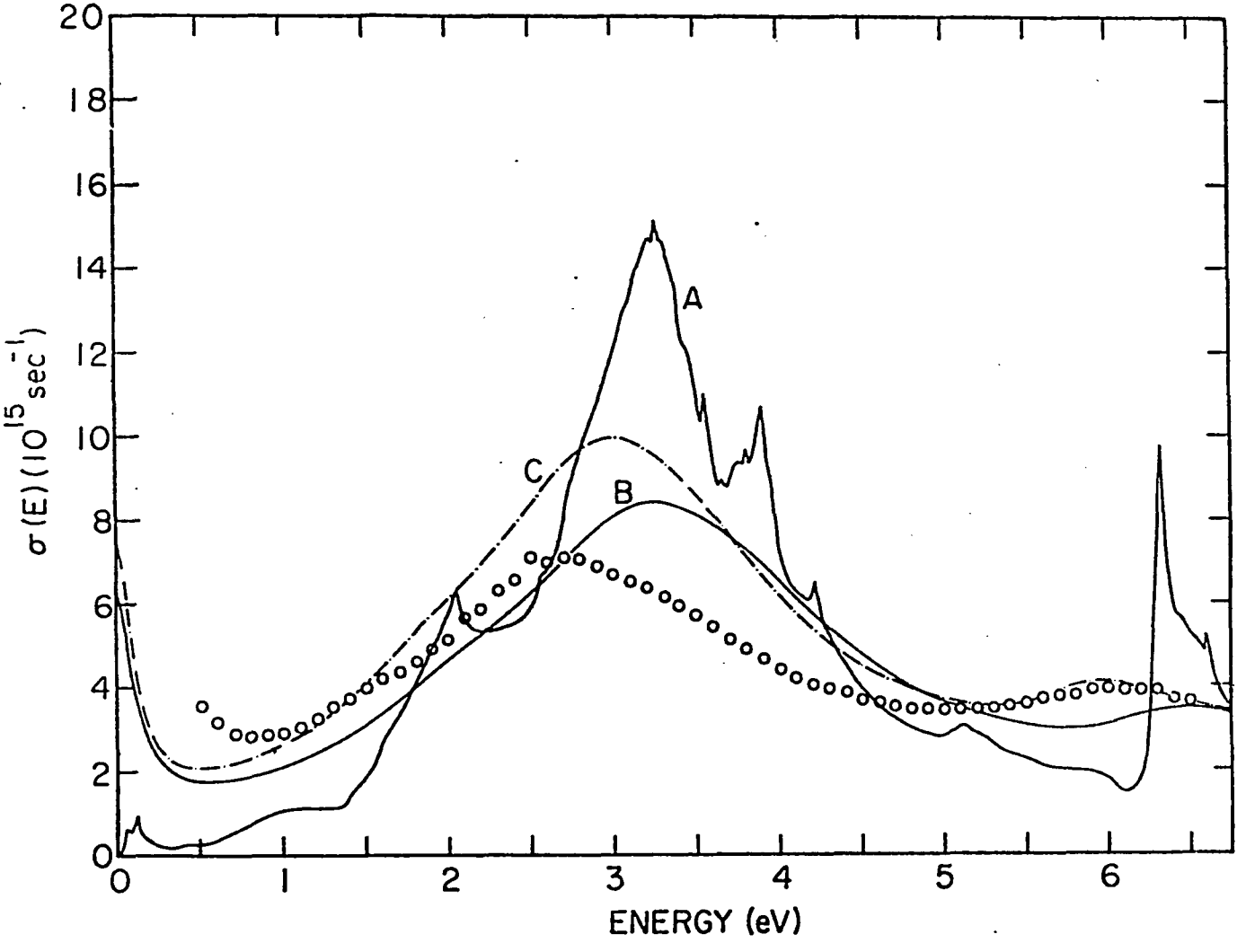

Figure XVII

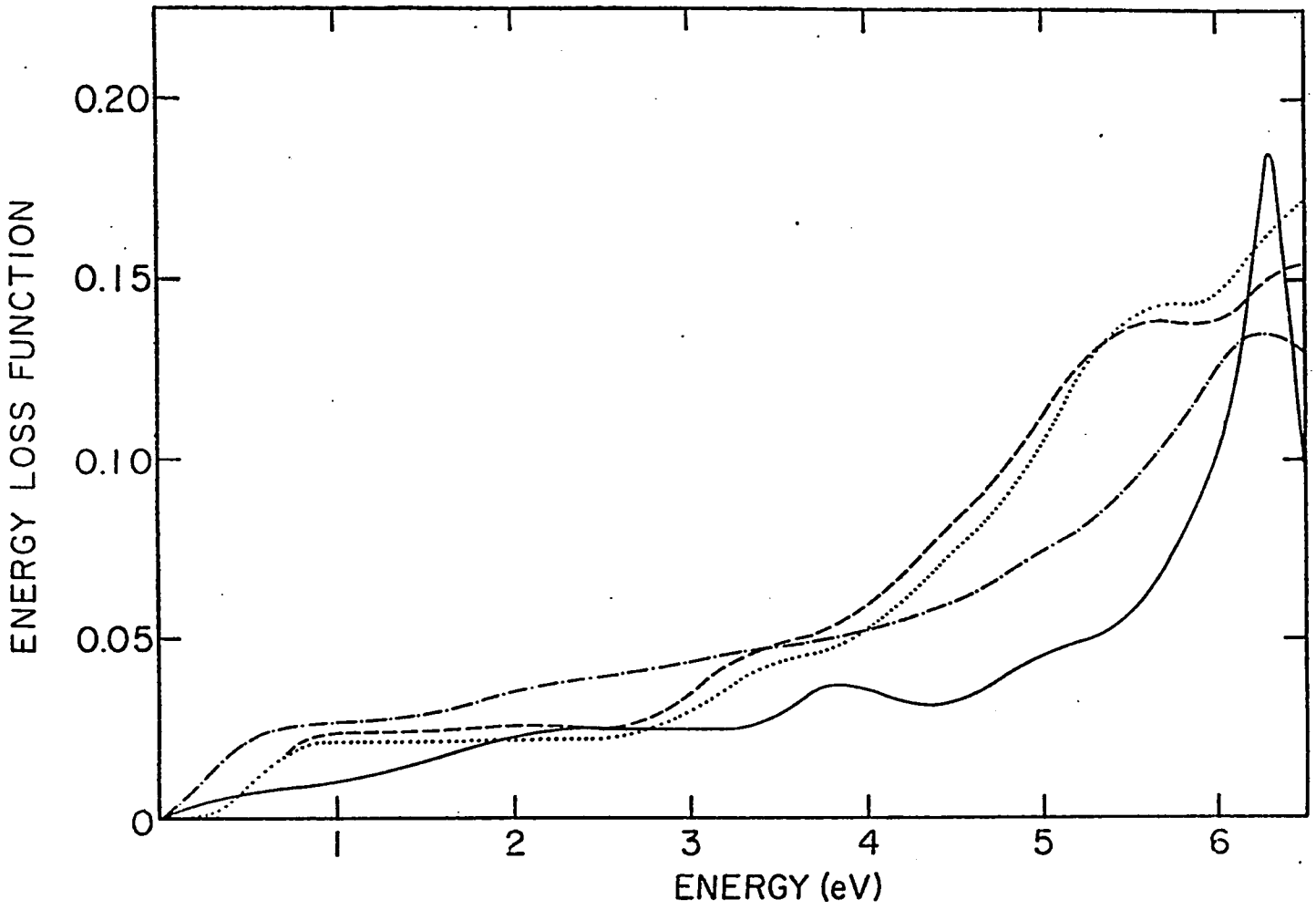

Figure XVIII

APPENDIX A

A. Angle-Resolved Photoemission Data Analysis

In the photoemission process, an incident photon transfers enough energy to an electron to enable it to overcome the potential barriers and exit from the solid as a free particle. Measurements of the emitted-electron energy spectrum provide an indication of the energy distribution of the electrons inside of the solid. Present experiments usually concentrate on emission normal to the surface of the solid and use several different photon energies. Synchrotron radiation has proven to be ideal for this purpose since it is intense and tunable over a reasonably wide energy range.

In a photoemission experiment, the kinetic energy

$$E_K = (\hbar^2/2m)K^2 \tag{A1}$$

of the emitted electrons and the angle of emission are measured. Conservation of energy requires that the energies of the initial and final (Bloch) states obey the relation

$$E_f(\vec{k}) = E_i(\vec{k}) + \hbar\omega \tag{A2}$$

where $\hbar\omega$ is the energy of the incident photon. In the three-step model of photoemission used by Berglund and

Spicer,[32] the electron (1) absorbs the photon, (2) travels from its position in the bulk to the surface and then (3) emerges from the sample. The measured kinetic energy is then

$$E_k = E_f(\vec{k}) - E_v \tag{A3}$$

where the vacuum-level energy is defined as

$$E_v = E_f + \Phi$$

where Φ is the work function of the face of the sample from which the electron emerged. Then the bulk energy bands are given by

$$E_i(\vec{k}) = E_k + Ef + \Phi - \hbar\omega$$

Even if the quantities to the right of the equal sign are known, we still do not know the position in $\vec{k}$-space we are scanning.

If the photoemission process conserved wave vector, the analysis would be trivial. However, only the tangential (to the surface) component is conserved

$$\vec{K}_t = \vec{k}_t + \vec{G} \tag{A4}$$

where $\vec{G}$ is a reciprocal lattice vector parallel to the surface. Thus, after combining equations (A1-A4), the result is

$$(\hbar^2/2m)K_n^2 = E_f(\vec{k}) - E_v - (\hbar^2/2m)(\vec{k}_t + \vec{G})^2 \qquad (A5)$$

Note that this does <u>not give a condition</u> on the normal component of $\vec{k}$

$$\vec{k}_n = \vec{k} - \vec{k}_t$$

For two-dimensional systems (such as surfaces), this poses no problem since the band structure is only weakly dependent upon $\vec{k}_n$. But in order to interpret the data for a (three-dimensional) solid, we need more information. The experimental procedure of holding the energy and the direction of emission constant and sweeping the energy of the incident photon supplies that needed information. This process fixes $\vec{K}_t$ and allows a sampling of $E_i(\vec{k})$ along suitable symmetry lines (parallel to the surface).

The procedure that has been used to date is to obtain a calculated band structure covering the range of photon energies used in the experiment (typically 10 to 30 eV). From this calculation, an "allowed" final state is chosen. An "allowed" state must be (1)

free-electron-like, and (2) allowed as a final state by symmetry (i.e., have a non-zero dipole matrix element with the initial state). The hope is that only one allowed final state exists in this range. For the (110) surface of chromium, a state of Σ_1 symmetry satisfies these conditions if the initial states are Σ_1, Σ_3, G_1, G_3 or G_4. Unfortunately, there are also two other allowed final states. This could cause tremendous complications except for the fact that they affect only the higher photon energies (above 23-24 eV) and can be ignored for moderate energies (15 to 23 eV).

The allowed band is fit to a free-electron-like (parabolic) dispersion relation

$$E = a\, k_n^2 + b \tag{A4}$$

which is then inverted to allow calculation of $|\vec{k}_n|$ from the observed energies.

$$|\vec{k}_n| = ((E - b)/a)^{\frac{1}{2}}$$

A simple least-squares procedure is sufficient for this fit. Then the value of $|\vec{k}_n|$ is brought into the irreducible wedge and this determines the position along the axis in question. The interesting point is that the value of $|\vec{k}_n|$ obtained in this way is relatively insensitive to the actual energy bands used in the fit

although the values of a and b vary quite a bit as illustrated in the following table:

Coefficients	Ref. 60	Present
a	0.0063 Ryd	0.00673 Ryd
b	-0.3882 Ryd	-0.64788 Ryd

APPENDIX B

B. The Self-Energy Correction

The work of Hohenberg and Kohn[90] and Kohn and Sham[1] has shown that all of the properties of the ground state of a solid may be obtained from a knowledge of the electronic charge density of the system. However, optical transitions depend upon the excited states of the system. Sham and Kohn[91] have shown that the excited-state energies $\tilde{E}_n(\vec{k})$ can be obtained from the eigenvalues $E_n(\vec{k})$ of the ground-state system by the formula

$$\tilde{E}_n(\vec{k}) = E_n(\vec{k}) + \lambda_n(\vec{k})\,(E_n(\vec{k}) - Ef) \qquad (B1)$$

where

$$\lambda_n(\vec{k}) = \frac{\int d\vec{r}\,|\psi_n(\vec{k},\vec{r})|^2\,(1 - m^*(\rho(\vec{r})))}{\int d\vec{r}\,|\psi_n(\vec{k},\vec{r})|^2\,m^*(\rho(\vec{r}))}$$

This same result is derivable from the expression given by Hedin and Lundquist[49] and is applicable when the density is slowly varying and for low-lying (near the Fermi energy) excited states. The factor $m^*(\rho(\vec{r}))$ is the effective mass (in units of the free electron mass) for the interacting electron gas as a functional of the ground-state charge density $\rho(\vec{r})$. As usual, $\psi_n(\vec{k},\vec{r})$ refers to the ground-state wavefunction.

The calculation of $\lambda_n(\vec{k})$ would be a very complex and time-consuming operation. Thus, as a first (and rather crude) approximation, it is taken to be real and independent of both $\vec{k}$ and n. Then Equation (B1) reduces to

$$\tilde{E}_n(\vec{k}) = E_n(\vec{k}) + \lambda(E_n(\vec{k}) - Ef)$$

Janak, Williams and Moruzzi[85] choose λ by matching calculated energies to observed optical transition energies while we use λ as a fitting parameter for the optical conductivity function. Both choices produce values in the same range ($|\lambda| \simeq 0.1$). This assumption has the same effect as defining an energy-dependent excited-state exchange-correlation potential

$$V_{xc}(\vec{r},E) = \mu_{xc}(\vec{r}) + \frac{\lambda}{1+\lambda}(E - Ef)$$

where $\mu_{xc}(\vec{r})$ is the ground-state exchange-correlation potential. If $V_{xc}(\vec{r},E)$ were used in a calculation instead of $\mu_{xc}(\vec{r})$, the energies would obey Equation (B2) and the wavefunctions would be unchanged since the energy-dependent term $(\lambda/(1+\lambda)(E-Ef))$ is independent of position. Since the wavefunctions do not change, the momentum matrix elements required of all optical-transition calculations may evaluated in the ground state. Thus, the only change in the expression for the optical

conductivity (Equation (9)) is that

$$\omega_{n\ell}(\vec{k}) \rightarrow \tilde{\omega}_{n\ell}(\vec{k}) = (1+\lambda)\,\omega_{n\ell}(\vec{k})$$

Thus, the delta function in that equation becomes

$$1/(1+\lambda)\ \delta(\omega_{n\ell}(\vec{k}) - \omega/(1+\lambda))$$

and an additional factor of $1/(1+\lambda)$ is obtained from the $1/\omega$ term, giving the required result

$$\tilde{\sigma}(\omega) = 1/(1+\lambda)^2\ \sigma(\omega/(1+\lambda)) \qquad \text{(B3)}$$

The entire analysis just discussed depends upon the validity of equation (B2). For energies that are too far from the Fermi energy, we expect equation (B2) to fail since the effects of exchange and correlation become negligible at very high energies. However, the results have been used at energies as high as 25 eV above the Fermi energy for copper with no indication of failure in this manner. Unfortunately, the situation is not as simple for the other 3d metals that have been investigated with this method. The earlier investigations of iron and nickel as well as the present work suggest that taking λ as a constant is <u>not</u> a good approximation for these materials. This may be due to

significant deviations of the effective mass (ratio) from 1 which do not occur for copper.

VITA

Duane Giles Laurent was born on December 17, 1952 in New Orleans, Louisiana and was raised in Reserve, Louisiana. He attended St. Peter's Parochial School in Reserve and, while there, he was selected to attend the Governor's Program for Gifted Children. While attending Leon Godchaux High School, also located in Reserve, he was a member of the Key Club and Beta Club and received honors at several regional literary rallies and science fairs. He received an academic scholarship to attend Southeastern Louisiana University in Hammond, Louisiana, where he majored in Physics and minored in Mathematics. He graduated, cum laude, with a Bachelor of Science degree in 1974 and was honored as the Outstanding Graduating Senior by the Department of Chemistry and Physics. In the same year, he married the former Miss Susan Waguespack, also of Reserve, Louisiana and accepted a graduate teaching assistantship in the Department of Physics and Astronomy at Louisiana State University in Baton Rouge, Louisiana. In 1976, he participated in a NATO summer school on "Electrons in Finite and Infinite Structures" held in Ghent, Belgium. Since that time, he has studied the energy bands, Fermi surfaces and optical properties of the 3d transition-metal series. He has coauthored several papers on these

subjects and has twice presented papers at the meeting of the American Physical Society held annually in March.

He is currently a candidate for the degree of Doctor of Philosophy in the Department of Physics and Astronomy at Louisiana State University. His major field is theoretical solid-state Physics and he holds minors in Plasma Physics and Computer Science. He is a member of the American Physical Society, the Association for Computing Machinery and the American Radio Relay League. His current interests include semiconductor device modelling, amateur radio, music and personal computers.

EXAMINATION AND THESIS REPORT

Candidate: Duane G. Laurent

Major Field: Solid State Physics

Title of Thesis: Energy Bands in Some Transition Metals

Approved:

Major Professor and Chairman

Dean of the Graduate School

EXAMINING COMMITTEE:

Date of Examination: